JOURNAL OF GEOPHYSICAL RESEARCH, VOL. 106, NO. D6, PAGES 5385–5401, MARCH 27, 2001

GATOR-GCMM: A global- through urban-scale air pollution and weather forecast model 1. Model design and treatment of subgrid soil, vegetation, roads, rooftops, water, sea ice, and snow

Mark Z. Jacobson

Department of Civil and Environmental Engineering, Stanford University, Stanford, California

Abstract. A model that treats nesting of gas, size- and composition-resolved aerosol, radiative, and meteorological parameters from the global through urban scales (<5-km grid spacing) was developed. The model treats multiple one-way-nested layers and multiple air quality and meteorological domains in each layer between the global and the urban scales. This latter feature allows forecast of air pollution and weather at several urban or regional sites during the same simulation. Regardless of the number of domains used during a single continuous simulation, the central memory required never exceeds 1.5 times and 2.1 times that of the largest domain for gas and gas/aerosol simulations, respectively. A submodule was developed for all domains to treat ground temperatures, latent heat fluxes, and sensible heat fluxes over subgrid soil types (with and without vegetation), water, sea ice, and urban areas. Urban areas are divided into road surfaces, rooftops, vegetation, and bare soil. Snow is treated over all surface types. The global-through-urban model is applied in a companion paper to study elevated ozone, ozone in national parks, and weather during a field campaign in northern and central California.

1. Introduction

Limited-area models (LAMs) are used for predicting weather and air quality on urban and regional scales. Nesting is a common method of providing lateral boundary conditions for LAMs. Unfortunately, unless the largest LAM scale is the global scale, boundary conditions are still needed for the largest LAM domain. Thus, an ideal nested model uses a global model for boundary conditions around the largest LAM domain.

Two widely used limited-area meteorological models with nesting features are the Penn State University (PSU)/National Center for Atmospheric Research (NCAR) mesoscale model [*Anthes et al.*, 1987, MM4; *Grell et al.*, 1994, MM5] and the Colorado State University regional atmospheric modeling system (CSURAMS) [*Pielke et al.*, 1992; *Copeland et al.*, 1996]. Limited-area meteorological models have been nested with global models or observations to produce a variety of regional climate models (RCMs) [e.g., *Dickinson et al.*, 1989; *Giorgi and Bates*, 1989; *McGregor and Walsh*, 1993; *Juang and Kanamitsu*, 1994; *Marinucci et al.*, 1995; *Podzun et al*, 1995; *Giorgi and Marinucci*, 1996; *Dudek et al.*, 1996; *Giorgi and Mearns*, 1999; *Qian et al.*, 1999; *Leung and Ghan*, 1999; *McGregor*, 1997; *Jones et al.*, 1997; *Laprise et al.*, 1998].

Nested limited-area meteorological models have also been used to provide boundary conditions for limited-area chemical transport models (CTMs). In some cases, the CTM and mesoscale model have both been nested (although not necessarily occupying the same domains) [e.g., *Pleim et al.*, 1991; *Jakobs et al.*, 1995; *Odman and Ingram*, 1996; *Byun and Ching*, 1999; *McHenry et al.*, 1999]. In other cases, the meteorological model has been nested, but the CTM has occupied only the innermost meteorological-model domain [e.g., *DaMassa et al.*, 1996; *Qian and Giorgi* , 1999; *T. Umeda and P. T. Martien*, Evaluation of a data assimilation technique for a mesoscale meteorological model used for air quality modeling, *J. Appl. Meteorol.*, in review, 2001]. In other cases, the CTM has been nested [*Morris et al.*, 1992; *Kumar et al.*, 1994] or configured with heterogeneous grid spacing [*Mathur et al.*, 1992], and winds were obtained off line from meteorological observations or model predictions.

Although RCMs in use today treat meteorology from the global scale to resolutions of 20 km [*Marinucci et al.*, 1995], 45 km [*Laprise et al.*, 1998], or 50 km [*Jones et al.*, 1997; *Giorgi and Marinucci*, 1996], no RCM has treated meteorology, gas chemistry, or aerosols from the global to urban scale (<5 km). Similarly, whereas all nested mesoscale LAMs coupled with CTMs account for gas chemistry and some nested LAMs account for aerosols [e.g., *Byun and Ching*, 1999, EPA Models-3; *McHenry et al.*, 1999, EDSS], none treats nesting of aerosols, chemistry, or meteorology up to the global scale. Current nested models are also limited by computer memory. They either need a separate memory for each grid (limiting the number of grids on a machine) or require that simulations for a grid be completed and the code recompiled for the next grid to be solved.

For this work, a one-way nested model was designed to treat gases, size- /composition-resolved aerosols, radiation, and meteorology from the global to the urban (< 5 km) scales. The model runs over a single, continuous simulation, and regardless of the number of domains, the central memory required never exceeds about 1.5 and 2.1 times that of the largest domain for gas simulations and gas/aerosol simulations, respectively. The model accounts for radiative

Paper number 2000JD900560.
0148-0227/01/2000JD900560$09.00

feedback from photochemically active gases, size-resolved aerosols, and size-resolved liquid water and ice particles to meteorology on all scales. The model treats subgrid soil and surface classes, including rooftops and road surfaces for ground-temperature calculations. The model is described below and applied in *Jacobson* [this issue] to study elevated ozone layers, ozone in national parks, and weather in northern and central California.

2. Description of the Model

The model, GATOR-GCMM (gas, aerosol, transport, radiation, general circulation, and mesoscale meteorological) model, derives from a global model, GATORG (gas, aerosol, transport, radiation, and general circulation model) [*Jacobson*, 2000, 2001], and a regional model, GATORM (gas, aerosol, transport, radiation, and mesoscale meteorological model) [*Jacobson et al.*, 1996; *Jacobson*, 1997a, 1997b; 1998a, 1999b, 1999c]. The gas, aerosol, and radiative parts of the two models are the same, but the meteorological and transport parts differ. There is no a priori reason why the regional and global metorological parts cannot be the same (except that boundary conditions must differ).

GATOR-GCMM is a single, unified model where all processes are run on line. It uses one common block and has switches to run in global mode, regional mode, nested mode, and with/without gases, aerosols, radiation, meteorology, transport, deposition, cloud physics, surface processes, etc. The model allows any number (limited only by computer time) of one-way nested layers of domains between the global and the urban scales, and in each layer, any number of domains for both air quality and meteorological calculations. In all domains in all layers, the air quality and meteorological domains occupy the same space and have the same grid spacing, except that in all nonglobal domains, each meteorological domain contains two more rows and columns than each air quality domain. In this "buffer zone," topographic gradients are eliminated to dampen gravity-wave reflections at boundaries. The horizontal and vertical coordinates in all domains are the spherical and sigma-pressure coordinates, respectively.

The model is presently run without spin-up or data assimilation so, it is prognostic, except for the emission inventory. Data assimilation of meteorology is useful for hindcasting air quality, improving modeled meteorological fields, and extending the length of simulations, but disadvantages are that it makes analysis and correction of meteorological prediction errors difficult, since such errors are hidden during the assimilation. It also prevents the study of feedbacks between air quality and meteorology, since such feedbacks depend on natural responses.

Figure 1 shows the processes solved in GATOR-GCMM, and Table 1 compares features of this model with those of two other nested models. Below, each model component is discussed, except that aerosol processes are discussed in a manuscript in preparation. Time steps for model processes are listed in *Jacobson* [this issue, Table 1].

2.1. Gas Processes

Gas processes in GATOR-GCMM include emissions, photochemistry, heterogeneous chemistry, nucleation, condensation/evaporation, dissolution/evaporation, and dry deposition. These processes are solved in all domains. Area- and mobile-source emissions are placed in the bottom model layer of all domains. Point-source emissions are placed in a layer determined from the stack height and estimated plume rise of the emissions. The method of determining plume rise height is obtained from *Briggs* [1975].

Gas photochemistry and heterogeneous chemistry are solved with SMVGEAR II [*Jacobson*, 1995, 1998b]. In all domains, 115 gases, 220 kinetic reactions, and 27 photolysis reactions are treated, except that three additional photolysis reactions are solved for in the global domain, since the top of the global domain extends to 55 km, whereas the tops of the regional domains are limited here to 16 km. The kinetic reactions used found in *Jacobson* [1999a, reactions 1-220 of Appendix Table B.4, corrections given at http://efml.stanford.edu/FAMbook/FAMbook.html]. Photolysis reactions include reactions 297-326 for the global domain and all except reactions 297, 300, and 305 for the regional domains. The chemical mechanism described above was recently compared by *Liang and Jacobson* [2000] with smog-chamber data and with two other mechanisms. For this study, the only heterogeneous reaction considered is $N_2O_5(g) + H_2O(a) \rightarrow 2HNO_3(g)$.

Dry deposition velocities for gases are calculated as the inverse sum of three resistances [*Jacobson*, 1999a, equations 20.10*ff*]. The surface resistance treatment [*Wesely*, 1989; *Walmsley and Wesely*, 1996] depends on land cover type. Land cover categories at 1-km resolution were obtained from *USGS* [1999]. Table 2 summarizes the fractional coverage, over the globe, of each category, found from the data. The 24 USGS land cover classes are compressed into each of Wesely's 11 land cover categories in each cell in each domain for dry deposition calculations. Predicted deposition velocities over

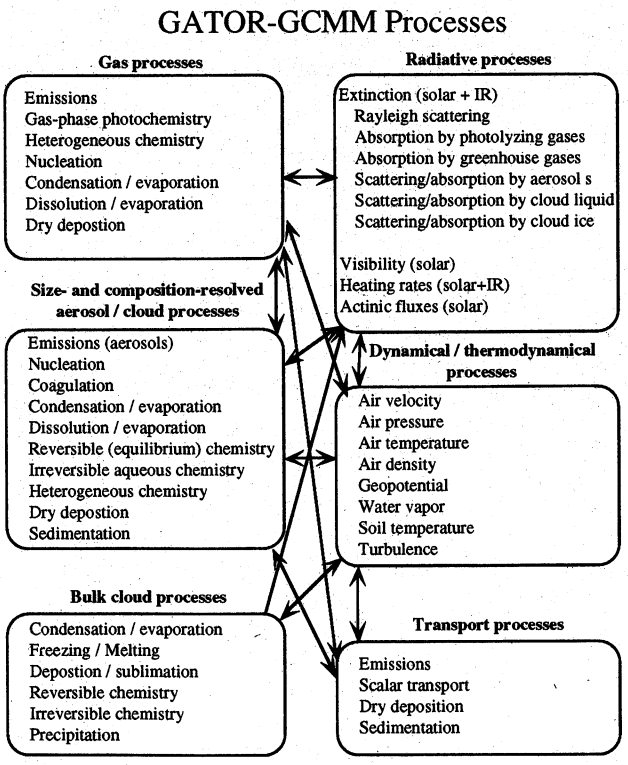

Figure 1. Processes and interactions in the GATOR-GCMM model.

each category in each cell are weighted by the fractional land cover of the category in the cell.

2.2. Radiative Transfer

Radiative transfer is used to determine diabatic heating rates for temperature calculations and actinic fluxes for photolysis calculations. Radiative calculations in the model depend on scattering and absorption by gases, aerosols, cloud liquid, and cloud ice. UV and visible gas absorption by all photolyzing gases, solar-IR absorption by H_2O, CO_2, O_3, and O_2 and thermal-IR absorption by H_2O, CO_2, O_3, CH_4, N_2O, $CFCl_3$, CF_2Cl_2, $CFCl_3$, and CCl_4 (with absorption coefficients from *Mlawer et al.* [1997]) are included.

Table 1. Identification of Major Features of a Global-to-Regional (RegCM), Regional-to-Urban (EPA Models-3), and Global-to-Urban (GATOR-GCMM) Nested Model

	RegCM	EPA Models-3	GATOR -GCMM
Recent reference	*Giorgi and Mearns* [1999]	*Byun and Ching* [1999]	this work
Chemical tracer model (CTM)?	---	yes	yes
Is the CTM nested?	---	yes	yes
Mesoscale meteorological model?	yes	yes	yes
Is the mesoscale model nested?	yes	yes	yes
Global meteorological model?	yes	---	yes
Gas processes			
gas photochemistry?	---	yes	yes
gas-to-particle conversion?	---	yes	yes
dry deposition?	---	yes	yes
photolysis feedback to weather?	---	---	yes
Aerosol processes		*	
prognostic number concentration?	---	---	yes
mass or mole concentration?	---	mass	mole
bins or modes	---	modes	bins
emissions?	---	yes	yes
nucleation?	---	yes	yes
coagulation?	---	yes	yes
condensational growth?	---	yes	yes
dissolutional growth?	---	---	yes
chemical equilibrium?	---	yes	yes
aerosol aqueous chemistry?	---	---	yes
sedimentation?	---	yes	yes
dry deposition?	---	yes	yes
aerosol feedback to radiation?	---	---	yes
Radiative transfer			
heating rates?	FMM	FMM	FRT
actinic fluxes?	---	LT	FRT
Rayleigh scattering?	yes	yes	yes
all photolyzing-gas absorption?	---	---	yes
greenhouse-gas absorption?	yes	yes	yes
aerosol scattering/absorption?	---	---	yes
cloud liq. scattering/absorption?	---	---	yes
cloud ice scattering/absorption?	---	---	yes
cloud fraction treatment?	yes	yes	---
Ground temperatures			
treatment of urban surfaces?	---	---	yes
treatment of subgrid soil types?	---	---	yes
Cloud processes			
cumulus parameterization?	yes	yes	yes
precipitation chemistry?	---	yes	yes
feedback to radiation?	TCF	TCF	TLI

FMM, from meteorological module calculation; FRT, from spectral radiative transfer calculation; LT, from lookup table; TCF, through cloud fraction; TLI, through liquid and ice size distributions.
**Binkowski and Shankar* [1995].

Table 2. Percent Global Land Cover for 24 USGS Categories

Land Cover Category	Percent
1, Urban and built-up land	0.051
2, Dryland cropland	2.137
3, Irrigated cropland	0.661
4, Mixed dry/irrig. cropland/pasture	0.000
5, Cropland/grassland mosaic	0.916
6, Cropland/woodland mosaic	1.813
7, Grassland	2.168
8, Shrubland	3.127
9, Mixed shrubland/grassland	0.267
10, Savanna	2.871
11, Deciduous broadleaf forest	1.223
12, Deciduous needleleaf forest	0.387
13, Evergreen broadleaf forest	2.529
14, Evergreen needleleaf forest	1.171
15, Mixed forest	1.222
16, Water bodies	71.32
17, Herbaceous wetland	0.060
18, Wooded wetland	0.195
19, Barren or sparsely vegetated	3.145
20, Herbaceous tundra	0.012
21, Wooded tundra	0.986
22, Mixed tundra	0.472
23, Bare ground tundra	0.009
24, Snow or ice	3.255

Data summed from 1-km global land cover data, as described in the text. The global data set did not include any pixels corresponding to category 4.

Cloud liquid and ice affect optics in each domain as follows: Bulk cloud liquid and ice contents from the cumulus parameterization are combined with modified-gamma size distribution data from *Welch et al.* [1980] and power-law/Marshall-Palmer distribution data from *Platt* [1997] for different cloud types to estimate cloud drop and ice crystal number and cross-sectional area distributions. Mie calculations are then combined with the distributions to give spectral cloud liquid and ice optical depths, single-scattering albedos, and asymmetry parameters, which are input into the radiative calculation. Surface albedos for the global domain are interpolated daily from a monthly averaged $1^\circ \times 1^\circ$ global data set [*NASA*, 1992], except that snow and sea-ice albedos are varied according to changes in modeled snow cover and sea-ice cover, respectively. Ground albedos for California are obtained from a 1-km resolution data set derived from AVHRR measurements for August, 1990 [*Martien and Umeda*, 1993]. Irradiances for diabatic heating rate calculations are determined for 86, 67, and 256 wavelength intervals in the regions <0.8, 0.8-4.5, and 4.5-1000 μm, respectively, with the radiative transfer algorithm described by *Toon et al.* [1989]. Actinic fluxes are determined for the 86 intervals in the region <0.8 μm.

2.3. Global Dynamics

The global dynamics module integrates equations for momentum (under the hydrostatic assumption), thermodynamic energy, and total water. The solution schemes originate from a 1994 version of the UCLA GCM [*Arakawa and Lamb*, 1977, 1981; *Arakawa and Suarez*, 1983]. The solution to the momentum equations is a fourth-order scheme that conserves potential enstrophy and energy [*Arakawa and Lamb*,

1981], designed to improve nonlinear aspects of flow over steep topography. The advection of thermodynamic energy and water are solved with a 13-point fourth-order scheme [*Arakawa*, 1995] that conserves the global mass integral of the square of the transported variable.

2.4. Global Transport

Transport of gases other than water vapor and transport of all aerosol components are performed with a code written here that uses the 13-point fourth-order scheme of *Arakawa* [1995]. The code was written to minimize redundant calculations when applied to different trace species. The scheme exactly conserves the constant mixing ratio of a species. Air density changes during advection of each species are also exactly consistent with air density changes during advection of momentum.

2.5. Regional Dynamics

The regional dynamics module integrates equations for momentum (under the hydrostatic assumption), thermodynamic energy, and total water. The hydrostatic assumption limits the accuracy of the model when the horizontal resolution is less than 3-4 km. The module was developed by *Lu and Turco* [1994, 1995] from finite-difference solutions to the momentum, thermodynamic energy, and water continuity equations by *Arakawa and Lamb* [1977] and *Arakawa and Suarez* [1983]. The solution to the momentum equations is a second-order scheme that conserves kinetic energy from inertial processes, integrated over the domain, and enstrophy during advection by the nondivergent part of the horizontal velocity. The difference scheme for advection of thermodynamic energy and water is second order in space. Lateral-boundary fluxes for all equations are determined from a mass-conservation relationship [*Arakawa*, 1982; *Lu and Turco*, 1994].

The regional dynamics module contains a hybrid boundary-layer turbulence scheme [*Lu and Turco*, 1994] in which three turbulence regimes are considered. Under strongly stable conditions, turbulence is suppressed and flow is assumed to be laminar. Under strongly unstable conditions, a convective plume model, which simulates rising convective turbulence and subsidence, is used to calculate turbulent fluxes and the height to which thermals accelerate buoyantly. Between these two limits, a first-order closure technique is used, and diffusion coefficients are calculated from *Blackadar* [1976].

2.6. Regional Transport

Transport of gases and aerosols in regional-scale domains is carried out with the scheme of *Walcek and Aleksic* [1998]. The scheme uses operator splitting and is monotonic (mixing ratios never fall below or rise above initial mixing ratios in current or neighboring cells during a time step) and exactly mass conserving. The scheme is absolutely monotonic for all dimensional flows, and constant mixing ratios are guaranteed to be maintained through a treatment of the density changes in each dimension of a multidimensional calculation. The scheme preserves peaks and odd shapes extremely well.

2.7. Cumulus Parameterization

The cumulus parameterization used for all nested domains is a modified *Arakawa and Schubert* [1974] algorithm developed by *Ding and Randall* [1998]. The algorithm allows cloud bases at any altitude; the original scheme allowed cloud bases in the boundary layer only. The modified scheme also accounts for downdrafts. The scheme predicts cumulus precipitation, liquid water and ice contents, and adjustments to large-scale potential temperature, momentum, and water vapor due to cumulus convection. The original UCLA GCM also included algorithms that estimated large-scale precipitation (large-scale plus cumulus precipitation is total precipitation), stratus cloud occurrence, and adjustments to large-scale potential temperature and water vapor due to stratus. These algorithms were retained here for the global domain and added to the regional domains. The stratus algorithm was modified to permit extraction of cloud liquid water and ice contents, which, along with cumulus liquid water and ice contents, were distributed over multiple size bins.

2.8. Nesting Boundary Conditions

When nesting is active, meteorological variables from a coarse domain are interpolated horizontally then vertically each nesting time interval (h_{nest}, typically 1800 s) to a boundary point inside a finer domain. In the horizontal, bilinear interpolation from four coarse-domain points to a fine-domain point is used. In the vertical, a logarithmic interpolation from two coarse-domain pressure points to a fine-domain pressure point is used. Interpolations are performed in the same manner between the global and the regional domains as they are between regional domains, and this is made easy by the fact that the global and regional dynamics schemes use the Arakawa C grid in the horizontal and the sigma-pressure coordinate in the vertical. As such, in the horizontal, potential temperatures and mixing ratios are interpolated from coarse to fine grid-cell centers, and u and v velocities are interpolated from coarse to fine cell edges.

At the end of each regional-domain dynamical time step (h_{dyn}, typically 4-6 s), variables inside the fine-domain boundary are relaxed to their values interpolated from the coarser domain (as described above) with [*Kurihara and Bender*, 1983; *Lu and Turco*, 1994]

$$\alpha_i = \frac{\alpha_o + f\alpha_i}{1+f}, \tag{1}$$

where α_i is the updated parameter value inside the fine-domain boundary, α_o is the parameter value interpolated from the coarse domain to the same position as α_i, and f is the relaxation coefficient. The relaxation time here is set to $f = \left(h_{\text{nest}} - h_{\text{dyn}}\right)/h_{\text{dyn}}$. For example, if $h_{\text{nest}} = h_{\text{dyn}}$, f=0, and $\alpha_i = \alpha_o$. The product fh_{dyn} is the e-folding lifetime for damping.

Boundary conditions for trace gases and aerosols differ somewhat from those for meteorological variables. The advection scheme used for regional transport [*Walcek and Aleksic*, 1998] requires mixing ratios at the horizontal center of a grid cell outside rather than inside a boundary. Thus, coarse-domain mixing ratios are interpolated to points outside, instead of inside, fine-domain points. The interpolation techniques used for meteorological variables are also used for gases and aerosols.

3. Surface Temperatures and Soil Moisture

An important parameter for predicting near surface air temperatures and pollutant concentrations is soil moisture [*Jacobson*, 1999c]. Soil moisture affects ground surface

temperatures, and both affect latent heat fluxes, sensible heat fluxes, and water vapor fluxes to the air. The inherent difficulty with treating ground temperatures is that a variety of surface covers and soil types must be considered.

For this work, a module was developed to treat ground temperatures over subgrid soil types (with and without vegetation), water, sea ice, and urban areas. Snow is treated over all surfaces. Accounting for subgrid heterogeneity over land is important, since soil parameterizations are tuned for specific soil types, yet grid cells in models contain many soil classifications. In the past, this problem was addressed by assuming a dominant soil type in a grid cell or averaging the soil parameters over all soil classifications. A problem with the first technique is that it does not account for the minority soil classes in a grid cell. Two problems with the second are that it is unclear how best to average certain soil parameters, such as exponential terms, and it is uncertain whether resulting averages have any physical meaning [e.g., *Kabat et al.*, 1997; *Dolman and Blyth*, 1997].

3.1. Treatment of Subgrid Heterogeneity

Ground temperatures over heterogeneous soil surfaces are treated as follows: First, each grid cell in each model domain is divided into as many as 15 surface classes, including 12 soil texture classes (sand, loamy sand, sandy loam, silt loam, loam, sandy clay loam, silty clay loam, clay loam, sandy clay, silty clay, clay, and organic matter) and three additional classes (liquid water, rooftops, and road surfaces). The fraction of each cell consisting of each soil class was derived for the United States from the 1 x 1 km data set of *Miller and White* [1998] and for the rest of the world from the 10 x 10 km data set of *Food and Agricultural Organization* (*FAO*) [1995]. Plate 1 shows maps of the dominant soil classes in each grid cell over a 4° x 5° global domain and a 0.05° x 0.05° northern California domain after the two data sets were merged. Whereas Plate 1 shows the dominant soil classes in each cell, each grid cell in the model consists of up to 15 surface classes. For fine-resolution domains (e.g., 5-km resolution) 2-7 surface classes exist in a grid cell. For coarse-resolution domains (e.g., 400-km global domains), a majority of surface classes exist in a grid cell.

Whether soil was covered by roofs or roads was estimated from the global 1 x 1 km AVHRR land cover data set discussed earlier. The data set contains 24 USGS land cover categories, including an "urban and built-up land" category. When a 1 x 1 km urban land cover square fell over a soil type, the soil was assumed to be covered by a specified fraction (section 3.3) of rooftop, road surface, vegetation, and bare soil.

Similarly, water bodies over soil were determined by laying the land cover data over the soil data. Although the soil data also contain water bodies, the resolution of the soil data was coarser than was that of the land cover data outside of the United States; thus, the land cover data set was used to determine the location of inland and coastal water. Water bodies from the soil data set that did not fall directly under higher-resolution water bodies from the land cover data set were filled in with the nearest soil class.

Once fractions of water, roofs, roads, and each soil class were known in each cell, the fractional vegetation (f_v) over each subgrid soil class was found. This was done by assigning a percent vegetation cover to each USGS land cover category, determining the category overlying each 1x1 km soil class, then summing and normalizing the product of the vegetation fraction and percent coverage of a particular land cover category over the soil class. The result was that in each grid cell, soil texture classes 1,...,12 were covered by a different percent vegetation. Parameters, such as leaf area index, canopy height, and minimum stomata resistance, were similarly obtained for each soil class in each grid cell.

The above information was then used during model simulations (where soil-module time steps were 10 s) to determine surface temperatures, sensible heat fluxes, latent heat fluxes, water vapor fluxes, friction velocities, etc., over each surface type in each grid cell of each domain. At the end of a step, each parameter was weighted by the fractional surface type in the cell to give an effective parameter value for the cell as a whole. In sum, instead of weighting individual soil parameters over all soil types in a cell, final products, such as ground temperatures and fluxes, were weighted. The averaging of, for example, latent heat fluxes from a lake, a sandy loam soil, roads, and roofs in a grid cell makes more physical sense than averaging properties of water, soil, roads and roofs, then calculating the flux on the basis of the average properties. Even the proposed treatment could be improved if subgrid variations in atmospheric parameters over each surface class were accounted for. Atmospheric variables are currently assumed to be an average over the grid cell as a whole. Below, the calculation of temperatures over different surface classes is discussed.

3.2. Soil Covered with Vegetation

For this work, a 10-layer bare-soil module originating from *Lu and Turco* [1994] was modified to treat vegetation and subgrid surface heterogeneity. The time-dependent equations solved in the below-surface module are the heat-conduction and liquid-water transport equations,

$$\frac{\partial T_{s,c}}{\partial t} = \frac{1}{\rho_{g,c} c_{g,c}} \frac{\partial}{\partial z}\left(\kappa_{s,c} \frac{\partial T_{s,c}}{\partial z} \right), \tag{2}$$

$$\frac{\partial w_{g,c}}{\partial t} = \frac{\partial}{\partial z}\left[K_{g,c}\left(\frac{\partial \psi_{p,c}}{\partial z} + 1 \right) \right] = \frac{\partial}{\partial z}\left(D_{g,c} \frac{\partial w_{g,c}}{\partial z} + K_{g,c} \right), \tag{3}$$

where the subscript c (used here) identifies the soil class in a particular grid cell, $T_{s,c}$ (K) is the sub-surface soil temperature in soil class c, $\kappa_{s,c}$ (J m^{-1} s^{-1} K^{-1}) is the thermal conductivity of the soil-water-air mixture, $\rho_{g,c}$ (kg m^{-3}) is the density of the mixture, $c_{G,c}$ (J kg^{-1} K^{-1}) is the specific heat of the mixture, $\kappa_{s,c}\partial T_{s,c}/\partial z$ (J m^{-2} s^{-1}) is the conductive heat flux through the soil-water-air mixture, $w_{g,c}$ (m^3 m^{-3}) is the volumetric water content of the soil (soil moisture), $K_{g,c}$ (m s^{-1}) is the coefficient of permeability of liquid water through the soil (hydraulic conductivity), $D_{g,c}$ (m^2 s^{-1}) is the diffusion coefficient for water in the soil, $\psi_{p,c}$ (m) is the moisture potential (soil-water tension), and $K_{g,c}\partial(\psi_{p,c}+z)/\partial z$ (m [m^3 m^{-3}] s^{-1}) is the kinematic flux of liquid water through the soil.

The expression used for the thermal conductivity (J m^{-1} s^{-1} K^{-1}) is [*McCumber and Pielke*, 1981]

$$\kappa_{s,c} = \max\left(418 e^{-\log_{10}|100\psi_{p,c}|-2.7}, 0.172 \right). \tag{4}$$

Clapp and Hornberger [1978] parameterized moisture potential, hydraulic conductivity, and the diffusion coefficient of water in soil with

$$\psi_{p,c} = \psi_{p,s,c}\left(\frac{w_{g,s,c}}{w_{g,c}} \right)^{b_c}, \tag{5}$$

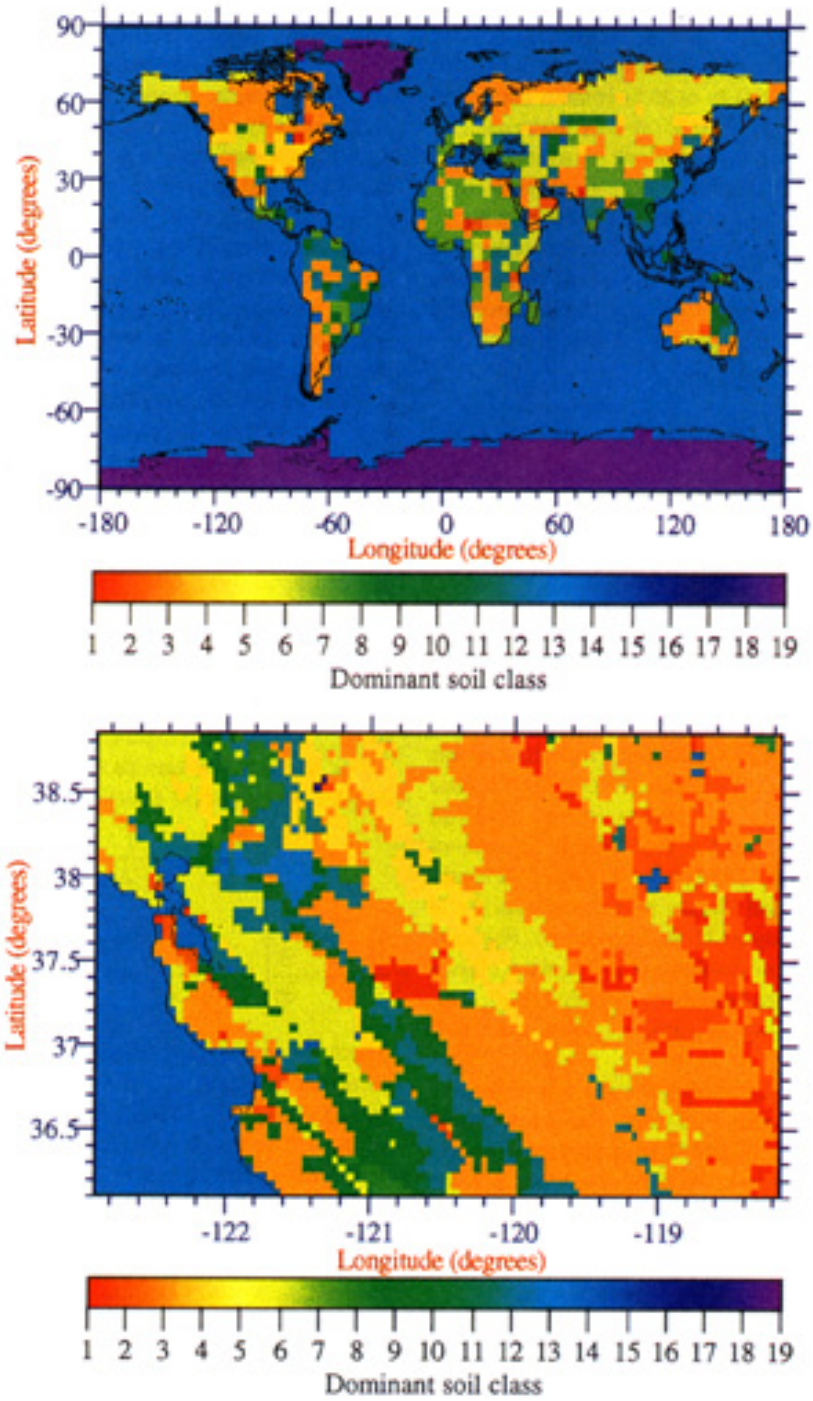

Plate 1. Dominant soil texture class in each grid cell of a 4°x5° global domain and a 0.05° x 0.05° northern California domain.

(1, sand; 2, loamy sand; 3, sandy loam; 4, silt loam; 5, silt; 6, loam; 7, sandy clay loam; 8, silty clay loam; 9, clay loam; 10, sandy clay; 11, silty clay; 12, clay; 13, peat; 14, water/sea ice; 15, bedrock; 16, other; 17, road surfaces; 18, rooftops; 19, snow).

$$K_{g,c} = K_{g,s,c}\left(\frac{w_{g,c}}{w_{g,s,c}}\right)^{2b_c+3}, \quad (6)$$

$$D_{g,c} = K_{g,c}\frac{\partial \psi_{p,c}}{\partial w_{g,c}} = -\frac{b_c K_{g,s,c}\psi_{p,s,c}}{w_{g,s,c}}\left(\frac{w_{g,c}}{w_{g,s,c}}\right)^{b_c+2}, \quad (7)$$

where $\psi_{p,s,c}$ (m) is the moisture potential at saturation, $w_{g,s,c}$ ($m^3\ m^{-3}$) is the volumetric water content at saturation, $K_{g,s,c}$ ($m\ s^{-1}$) is the hydraulic conductivity at saturation, and b_c is a fitting coefficient. The product of density and specific heat in (2) can now be written as $\rho_{g,c}c_{g,c} = (1-w_{g,s,c})\rho_{s,c}c_{s,c} + w_{g,c}\rho_w c_w$, where $\rho_{s,c}$ ($kg\ m^{-3}$) is the density of solid soil, $c_{s,c}$ ($J\ kg^{-1}\ K^{-1}$) is the specific heat of solid soil, ρ_w ($kg\ m^{-3}$) is the density of liquid water, and c_w ($J\ kg^{-1}\ K^{-1}$) is the specific heat of liquid water. Values of $\rho_{s,c}c_{s,c}$, $\psi_{p,s,c}$, $w_{g,s,c}$, $K_{g,s,c}$, and b_c used here are shown by *Jacobson* [1999a, Table 8.3] for different soil types.

Equations (2) and (3) were solved by *Lu and Turco* [1994] by dividing the subsurface into 10 layers of thickness (from top to bottom) of 0.005, 0.01, 0.01, 0.01, 0.015, 0.025, 0.05, 0.075, 0.10, and 0.20 m (thus, the deepest soil layer was 0.5 m below the surface), then writing the equations in central-difference form in space and Crank-Nicolson form in time and solving them as a tridiagonal matrix. No fluxes were allowed in or out of the bottom boundary, but each time step, the deepest soil moisture layer was reset to its initial value. Thus, a constant moisture source was assumed to exist at the bottom boundary.

At the top, the energy flux in (2), $\kappa_{s,c}\partial T_{g,c}/\partial z$ ($J\ m^{-2}\ s^{-1}$), is replaced by $F_{g,c} - H_{g,c} - L_e E_{g,c}$, accounting for radiative, sensible, and latent heat fluxes, and the moisture flux in (3) $D_{g,c}\partial w_{g,c}/\partial z + K_{g,c}$ ($m\ s^{-1}$) is replaced by $E_{g,c}$, accounting for condensation/evaporation. These terms were previously applied over one bare soil class per grid cell. Here, they are modified for subgrid soil, vegetation, urban surfaces, water, and sea ice, and snow over all surfaces. $F_{g,c}$ ($W\ m^{-2}$) is defined here as the net downward minus upward solar irradiance (positive is downward) over bare soil in soil class c at ground level plus the net downward minus upward thermal-infrared (thermal-IR) irradiance over bare plus vegetated soil in class c at ground level, $H_{g,c}$ ($W\ m^{-2}$) is the sensible heat flux between bare soil and open air plus that between vegetated soil and canopy air (positive is upward), L_e ($J\ kg^{-1}$) is the latent heat of evaporation, $E_{g,c}$ ($kg\ m^{-2}\ s^{-1}$) is the turbulent moisture flux between bare soil and open air or vegetated soil and canopy air (positive is upward), and $L_e E_{g,c}$ ($W\ m^{-2}$) is the latent heat flux.

The numerical solution to (2) gives temperatures in the middle of each subsoil layer, not at the soil surface. Surface temperatures can be obtained from a surface energy-balance equation that accounts for radiative, sensible heat, and latent heat fluxes between the ground and the air, and conductive heat fluxes between the top and the middle of the first soil layer. Vegetation modifies fluxes to and from the surface. In the presence of vegetation, the ground-surface energy balance is written as

$$F_{g,c} - H_{g,c} - L_e E_{g,c} + \kappa_{s,c,1}\frac{\partial T_{s,c}}{\partial z} = 0, \quad (8)$$

where $\kappa_{s,c,1}$ ($W\ m^{-1}\ K^{-1}$), from (4), is the thermal conductivity of a soil-water-air mixture in the top model-layer of soil. At the ground surface, $T_{s,c} = T_{g,c}$ (K), which is the average (over vegetated and nonvegetated soil) ground-top temperature for subgrid soil class c.

The fluxes in (8) are specified as

$$F_{g,c} = f_{s,c}\overline{F}_s + \overline{F}_i + \sigma_B\left(\overline{\varepsilon}\overline{T}_g^4 - \varepsilon_{s,c}T_{g,c}^4\right), \quad (9)$$

$$H_{g,c} = -f_{s,c}\frac{\overline{\rho}_a c_{p,d}}{R_{a,c}}\left[\overline{\theta}_p(z_r) - \frac{T_{g,c}}{\overline{P}_g}\right] - f_{v,c}\frac{\overline{\rho}_a c_{p,d}}{R_{f,c}}\left[\frac{T_{af,c}}{\overline{P}_f} - \frac{T_{g,c}}{\overline{P}_g}\right], \quad (10)$$

$$L_e E_{g,c} = -f_{s,c}L_e\frac{\overline{\rho}_a}{R_{a,c}}\beta_{g,c}\left[\overline{q}_v(z_r) - q_{v,s}\left(T_{g,c}\right)\right] - f_{v,c}L_e\frac{\overline{\rho}_a}{R_{f,c}}\beta_{g,c}\left[q_{af,c} - q_{v,s}\left(T_{g,c}\right)\right], \quad (11)$$

where $f_{s,c}$ and $f_{v,c}$ are the fractions of soil class c in the grid cell covered with bare soil and vegetated soil, respectively ($f_{s,c} + f_{v,c} = 1$), $\overline{F}_s$ ($W\ m^{-2}$) is the grid-cell-averaged net downward minus upward solar irradiance absorbed by the ground (positive is downward), $\overline{F}_i$ ($W\ m^{-2}$) is the grid-cell-averaged net downward minus upward thermal-IR irradiance absorbed by the ground (positive is downward), σ_B ($5.67051 \times 10^{-8}\ W\ m^{-2}\ K^{-4}$) is the Stefan-Boltzmann constant, $\overline{\varepsilon}$ is the grid-cell-averaged thermal-IR emissivity of bare and vegetated surfaces together, $\varepsilon_{s,c}$ is the thermal-IR emissivity of soil in soil class c, $\overline{T}_g$ (K) is the grid-cell-averaged (over all subgrid surface classes and vegetation covers) ground temperature, $\overline{\rho}_a$ ($kg\ m^{-3}$) is the grid-cell-averaged air density, $c_{p,d}$ ($J\ kg^{-1}\ K^{-1}$) is the specific heat of dry air at constant pressure, $R_{a,c}$ ($s\ m^{-1}$) is the aerodynamic resistance between bare soil outside of a canopy and a reference height z_r (m), $R_{f,c}$ ($s\ m^{-1}$) is the aerodynamic resistance between the vegetated soil and the overlying foliage, $\overline{\theta}_p(z_r)$ (K) is the grid-cell-averaged potential temperature at the reference height, $\overline{P}_g = \left[\overline{p}_{a,g}/1000\ \text{mbar}\right]^{\kappa}$ converts temperature at the ground to potential temperature (in this expression, $\overline{p}_{a,g}$ is air pressure at the surface in millibars and $\kappa = 0.286$), $\overline{P}_f = \left[\overline{p}_{a,f}/1000\ \text{mbar}\right]^{\kappa}$ converts temperature in the foliage to potential temperature, $T_{af,c}$ (K) is the temperature of air in the foliage, $\beta_{g,c}$ is a wetness function that accounts for resistance to vapor diffusion through soil macropores, $\overline{q}_v(z_r)$ ($kg\ kg^{-1}$) is the grid-cell-averaged water vapor mass mixing ratio at the reference height, $q_{v,s}\left(T_{g,c}\right)$ ($kg\ kg^{-1}$) is the saturation mixing ratio (over liquid or ice) at the ground temperature, and $q_{af,c}$ ($kg\ kg^{-1}$) is the mixing ratio of water vapor in foliage air.

Equation (9) accounts for net direct and diffuse solar radiation hitting bare soil and net infrared radiation over bare soil and soil underneath a canopy. It assumes that the net shortwave radiation reaching the ground in a canopy is small. *Pielke* [1984] found that this assumption is reasonable for dense forests, where only 6-8% of shortwave radiation reaches the surface. $\overline{F}_s$ and $\overline{F}_i$ in (9) are calculated with grid-cell-averaged emissivities and ground temperatures, $\overline{\varepsilon}$ and $\overline{T}_g$, respectively. Thus in (9), the grid-cell-averaged ground emission term is first subtracted from the downward-oriented $\overline{F}_i$, then a ground radiative emissions term over the current soil class is added back to give a better estimate of the net radiation reaching the soil. The first terms on the right-hand sides of (10) and (11) account for fluxes to/from bare soil and the second terms account for fluxes to/from vegetated soil.

The expression for $\beta_{g,c}$ used in (11) is

$$\beta_{g,c} = \begin{cases} \frac{1}{4}\left[1-\cos\left(\frac{w_{g,c}}{w_{fc}}\pi\right)\right]^2 & w_{g,c} < w_{fc} \\ 1 & w_{g,c} \geq w_{fc} \text{ or } \overline{q}_v(z_r) > q_{v,c}(z_{0,v}) \end{cases}, \quad (12)$$

from *Lee and Pielke* [1992], who obtained the fit from data of *Kondo et al.* [1990]. Here, $w_{g,c}$ (m^3 m^{-3}) is the soil liquid water content (LWC) of the top soil layer and w_{fc} (m^3 m^{-3}) is the soil LWC at field capacity, which is the LWC after all macropores of soil have emptied due to gravitational drainage and liquid water remains only in soil micropores. When condensation occurs, and for water, ice, and snow surfaces, $\beta_{g,c}$=1.

The aerodynamic resistance (s m^{-1}) over bare soil in (10) and (11) is calculated as

$$R_{a,c} = \frac{\int_{z_{0,h}}^{z_r} \phi_{h,c} \frac{dz}{z}}{k u_{*,c}}, \quad (13)$$

where k is the von Kármán constant, $u_{*,c}$ is the friction velocity (m s^{-1}) over soil class c, $\phi_{h,c}$ is the dimensionless potential temperature gradient, and $z_{0,h}$ (m) is the roughness length for energy. A roughness length and dimensionless gradient for moisture should be used in (13), but these parameters are often assumed to equal the corresponding energy parameters. The integral of $\phi_{h,c}$ is calculated with (8.25) of *Jacobson* [1999a], derived from equations of *Businger et al.* [1971] and parameters of *Hogstrom* [1988]. $\theta_{*,c}$ and $u_{*,c}$ are calculated from the parameterization of *Louis* [1979], as shown by *Jacobson* [1999a, equations 8.27-8.29]. Whereas, an advantage of the Louis method is that it is noniterative, a disadvantage is that it assumes that the surface roughness length for energy equals that for momentum, which is incorrect and a source of some model error. An alternative is an iterative calculation involving $\theta_{*,c}$, $u_{*,c}$, and the Monin-Obukhov length.

The surface roughness length for momentum over the ocean in the model is determined from $0.013u_{*,c}^2/g + 0.11\nu/u_{*,c}$ [*Zeng et al.*, 1998], where g is gravitational acceleration (m s^{-2}) and ν is the kinematic viscosity of air (m^2 s^{-1}). The roughness length over land was determined from $z_2\left(1-0.91e^{-0.0075L_{T,c}}\right)$ [*Sellers et al.*, 1996], where z_2 is the canopy height (m), and $L_{T,c}$ is the one-sided leaf area index (square meters of leaf surfaces per square meter of underlying ground). Canopy heights for each land use/land cover category are estimated by *Sellers et al.* [1996, Table 5]. $L_{T,c}$ values are estimated as $7f_{v,c}$. *Deardorff* [1978] argued that $7f_{v,c}$ must be an upper limit, since at higher values, insufficient light is available to support further growth in a canopy. Zero-plane displacement heights are set to three-quarters of canopy heights [e.g., *Deardorff*, 1978; *Pielke*, 1984].

In the foliage, the aerodynamic resistance (s m^{-1}) is calculated as

$$R_{f,c} = \frac{1}{c_f u_{af}}, \quad (14)$$

where $u_{af} \approx 0.83u_*$ (m) is the wind speed in the foliage and $c_f = 0.01 - 0.003/u_{af}$ (u_{af} in meters) is the dimensionless heat-transfer coefficient [e.g., *Deardorff*, 1978; *Pielke*, 1984].

The two remaining terms needed in (10) and (11) are the temperature and mixing ratio of air in the foliage. These parameters were estimated by *Deardorff* [1978] as

$$T_{af,c} = 0.3\overline{T}_a(z_r) + 0.6T_{f,c} + 0.1T_{g,c}, \quad (15)$$

$$q_{af,c} = 0.3\overline{q}_v(z_r) + 0.6q_{f,c} + 0.1q_{g,c}, \quad (16)$$

where $\overline{T}_a(z_r)$ (K) and $\overline{q}_v(z_r)$ (kg kg^{-1}) are the grid-cell-averaged temperature and mixing ratio, respectively, at the reference height, $T_{f,c}$ and $q_{f,c}$ are the temperature and water vapor mixing ratio, respectively, in leaf stomata, and $T_{g,c}$ and $q_{g,c}$ are the temperature and water vapor mixing ratio, respectively, in soil macropores. These equations require two further terms, $T_{f,c}$ and $q_{f,c}$. The latter term was calculated by *Deardorff* [1978] as

$$q_{f,c} = \min\left[\gamma q_{v,s}(T_{f,c}) + (1-\gamma)q_{af,c}, q_{v,s}(T_{f,c})\right], \quad (17)$$

where

$$\gamma = \begin{cases} \frac{R_{f,c}}{R_{f,c}+R_{st,c}}\left[1-\left(\frac{W_c}{W_{\max,c}}\right)^{2/3}\right] & q_{af,c} < q_{v,s}(T_{f,c}) \\ 0 & q_{af,c} \geq q_{v,s}(T_{f,c}) \end{cases}. \quad (18)$$

In this equation, W_c (m^3 m^{-2} or m) is the depth of liquid water on an individual leaf surface (m) multiplied by the one-sided leaf area index, $L_{T,c}$ (square meters of leaf surfaces per square meter of underlying ground), and $W_{\max,c}$ (m) is the maximum possible value of W_c, A prognostic equation for W_c is given shortly. $W_{\max,c}$ is assumed to be $0.0002L_{T,c}$ (m) [*Dickinson*, 1984]. In (18), $R_{st,c}$ (s m^{-1}) is the leaf stomata resistance, given as [*Baldocchi et al.*, 1987]

$$R_{st,c} = \frac{R_{\min,c}}{F_c}\left[1+\left(\frac{200}{\overline{F}_s+0.1}\right)^2\right]\frac{400}{\overline{T}_{sa,C}\left(40-\overline{T}_{sa,C}\right)}, \quad (19)$$

where $R_{\min,c}$ is the minimum bulk canopy stomata resistance, obtained here from *Wesely* [1989] for several land cover categories and seasons, $\overline{T}_{sa,C}$ is the grid-cell and time-step averaged surface air temperature (°C), and

$$F_c = \max\left[\min\left(\frac{w_{g,\text{avg},c} - w_{\text{wilt},c}}{w_{cr,c} - w_{\text{wilt},c}}, 1.0\right), 1.0\times10^{-12}\right] \quad (20)$$

is a factor accounting for loss of transpiration due to drying up of the soil toward the wilting point, $w_{\text{wilt,c}}$ (m^3 m^{-3}) [e.g., *Noilhan and Planton*, 1989]. In this equation, $w_{g,\text{avg},c}$ (m^3 m^{-3}) is the average liquid water content in the root layers of soil, and $w_{cr,c}$ (m^3 m^{-3}) is a critical liquid-water content taken as $0.75w_{g,s,c}$ [*Thompson et al.*, 1981], where $w_{g,s,c}$ (m^3 m^{-3}) is the soil moisture content at saturation. In (19), $R_{st,c}$ is assumed to be infinite when $\overline{T}_{sa,C} \leq 0$°C and $\overline{T}_{sa,C} \geq 40$°C and is predicted to be large at nighttime, when $\overline{F}_s$ is zero. When water transpires through leaf stomata, 30% is removed from model soil layers above a soil depth of 0.1 m and the rest is removed from model soil layers below this depth, down to 1.5 m for forests and 1.0 m for grassland [*Sellers et al.*, 1996].

The foliage temperature $T_{f,c}$ must be computed iteratively by solving a foliage energy balance equation that considers net solar fluxes at the top of the foliage, net thermal-IR fluxes at the top of the foliage and at ground level, and sensible and latent heat fluxes at the top of the foliage and at ground level [e.g., *Deardorff*, 1978; *McCumber*, 1980; *Pielke*, 1984]. The equation solved here is

$$f_{v,c}\left[\overline{F}_s+\varepsilon_{v,c}F_{i,c}\downarrow+\frac{\varepsilon_{v,c}\varepsilon_{s,c}}{\varepsilon_{v,c}+\varepsilon_{s,c}-\varepsilon_{v,c}\varepsilon_{s,c}}\sigma_B T_{g,c}^4\right.$$

$$\left.-\frac{\varepsilon_{v,c}+2\varepsilon_{s,c}-\varepsilon_{v,c}\varepsilon_{s,c}}{\varepsilon_{v,c}+\varepsilon_{s,c}-\varepsilon_{v,c}\varepsilon_{s,c}}\varepsilon_{v,c}\sigma_B T_{f,c}^4\right]$$

$$=H_{v,c}+L_eE_{d,c}+L_eE_{t,c}, \tag{21}$$

where $\varepsilon_{v,c}$ is the thermal-IR emissivity of vegetation over soil class c, $F_{i,c}\downarrow$ (W m^{-2}) is the downward thermal-IR irradiance at the top of the canopy over soil class c, $H_{v,c}$ (W m^{-2}) is the sensible heat flux between air in the foliage and leaves, $E_{d,c}$ (kg m^{-2} s^{-1}) is the turbulent moisture flux due to direct evaporation from/condensation to leaves in the foliage, and $E_{t,c}$ (kg m^{-2} s^{-1}) is the turbulent moisture flux due to transpiration from leaf stomata. The downward thermal-IR irradiance over soil class c is calculated as

$$F_{i,c}\downarrow=\frac{\overline{F}_i+\overline{\varepsilon}\sigma_B\overline{T}_g^4}{\overline{\varepsilon}}. \tag{22}$$

The sensible heat flux, direct evaporation/condensation, and transpiration terms in (21) are

$$H_{v,c}=-1.1L_{T,c}\frac{\overline{\rho}_a c_{p,d}}{R_{f,c}\overline{P}_f}\left[T_{af,c}-T_{f,c}\right], \tag{23}$$

$$E_{d,c}=-L_{T,c}\frac{\overline{\rho}_a\beta_d}{R_{f,c}}\left[q_{af,c}-q_{v,s}\left(T_{f,c}\right)\right], \tag{24}$$

$$E_{t,c}=-L_{T,c}\frac{\overline{\rho}_a(1-\beta_d)}{R_{f,c}+R_{st,c}}\left[q_{af,c}-q_{v,s}\left(T_{f,c}\right)\right], \tag{25}$$

respectively, where the factor 1.1 in (23) accounts for the effects of stalks, stems, twigs, and limbs that exchange energy but do not transpire, and

$$\beta_d=\begin{cases}\left(\dfrac{W_c}{W_{\max,c}}\right)^{2/3} & q_{af,c}<q_{v,s}\left(T_{f,c}\right)\\ 1 & q_{af,c}\geq q_{v,s}\left(T_{f,c}\right)\end{cases}, \tag{26}$$

accounts for the decrease in the evaporation rate when the leaves contain little water [*Deardorff*, 1978]. During condensation, direct moisture flux to leaf surfaces via (24) occurs at the potential rate (β_d=1). When dew condenses on leaves, $1-\beta_d$=0 and no transpiration occurs by (25). When direct evaporation occurs, the transpiration rate is limited by the fraction of leaf surfaces not covered by liquid water. The saturation mixing ratios in (24) and (25) are at the temperature of the foliage, determined from (21).

Equation (21) is solved iteratively for $T_{f,c}$ by substituting (23)-(25) into it, then linearizing $T_{f,c}^4$ and $q_{v,s}\left(T_{f,c}\right)$ with

$$T_{f,c,t,n+1}^4=T_{f,c,t,n}^4+4T_{f,c,t,n}^3\left(T_{f,c,t,n+1}-T_{f,c,t,n}\right), \tag{27}$$

$$q_{v,s}\left(T_{f,c,t,n+1}\right)=q_{v,s}\left(T_{f,c,t,n}\right)+\frac{dq_{v,s}\left(T_{f,c,t,n}\right)}{dT}\left(T_{f,c,t,n+1}-T_{f,c,t,n}\right), \tag{28}$$

respectively [*Deardorff*, 1978], where the subscript t indicates a value at the end of the time step and the subscript n indicates iteration number. Applying these steps gives the foliage temperature as

$$T_{f,c,t,n+1}=$$

$$\frac{\left\{f_{v,c}\left[\begin{array}{l}\overline{F}_s+\varepsilon_{v,c}F_{i,c}\downarrow+\dfrac{\varepsilon_{v,c}\varepsilon_{s,c}}{\varepsilon_{v,c}+\varepsilon_{s,c}-\varepsilon_{v,c}\varepsilon_{s,c}}\sigma_B T_{g,c,t-h}^4\\ +3\dfrac{\varepsilon_{v,c}+2\varepsilon_{s,c}-\varepsilon_{v,c}\varepsilon_{s,c}}{\varepsilon_{v,c}+\varepsilon_{s,c}-\varepsilon_{v,c}\varepsilon_{s,c}}\varepsilon_{v,c}\sigma_B T_{f,c,t,n}^4\end{array}\right]\right.}{\left.+1.1L_{T,c}\dfrac{\overline{\rho}_a c_{p,d}}{R_{f,c}\overline{P}_f}T_{af,c}+L_eL_{T,c}\overline{\rho}_a\left\{\dfrac{\beta_d}{R_{f,c}}+\dfrac{\overline{\rho}_a\beta_t}{R_{f,c}+R_{st,c}}\right\}\right\}}$$

$$\times\left[q_{af,c}-\left\{q_{v,s}\left(T_{f,c,t,n}\right)-\frac{dq_{v,s}\left(T_{f,c,t,n}\right)}{dT}T_{f,c,t,n}\right\}\right]$$

$$\left\{\begin{array}{l}4\dfrac{\varepsilon_{v,c}+2\varepsilon_{s,c}-\varepsilon_{v,c}\varepsilon_{s,c}}{\varepsilon_{v,c}+\varepsilon_{s,c}-\varepsilon_{v,c}\varepsilon_{s,c}}\varepsilon_{v,c}\sigma_B T_{f,c,t,n}^3+1.1L_{T,c}\dfrac{\overline{\rho}_a c_{p,d}}{R_{f,c}\overline{P}_f}\\ +L_eL_{T,c}\overline{\rho}_a\left\{\dfrac{\beta_d}{R_{f,c}}+\dfrac{\overline{\rho}_a(1-\beta_d)}{R_{f,c}+R_{st,c}}\right\}\dfrac{dq_{v,s}\left(T_{f,c,t,n}\right)}{dT}\end{array}\right\}, \tag{29}$$

where the subscript t-h indicates a value at the beginning of a time step. Equation (29) needs to be iterated only four times in the model to achieve significant convergence.

One more equation needed before ground temperatures can be predicted is a prognostic equation for water on leaf surfaces. Such an equation is

$$\frac{\partial W_c}{\partial t}=\overline{P}_r-\frac{E_{d,c}}{\rho_w}-R, \tag{30}$$

where $\overline{P}_r$ (m s^{-1}) is the grid-cell and time-averaged rainfall precipitation rate, ρ_w (kg m^{-3}) is the temperature-dependent density of liquid water, and R (m s^{-1}) is the runoff rate from leaf surfaces. Substituting (26) into (24) and (24) into (30) and finite-differencing the result over time step h (s), where t-h and t are initial and final times, respectively, gives

$$W_{c,t}=W_{t-h,c}+\begin{cases}h\left(\overline{P}_r+\dfrac{L_{T,c}}{R_{f,c}}\dfrac{\overline{\rho}_a}{\rho_w}\left(\dfrac{W_{c,t-h,c}}{W_{\max,c}}\right)^{\frac{2}{3}}\left[q_{af,c}-q_{v,s}\left(T_{f,c}\right)\right]\right) & q_{af,c}<q_{v,s}\left(T_{f,c}\right)\\ h\left(\overline{P}_r+\dfrac{L_{T,c}}{R_{f,c}}\dfrac{\overline{\rho}_a}{\rho_w}\left[q_{af,c}-q_{v,s}\left(T_{f,c}\right)\right]\right) & q_{af,c}\geq q_{v,s}\left(T_{f,c}\right)\end{cases} \tag{31}$$

The solution is limited by $W_c=\min\left(\max\left[W_c,0\right],W_{\max,c}\right)$, which accounts for the fact that any liquid water over depth $W_{\max,c}$ is runoff [thus R does not appear in (31)]. Each solution from (31) is substituted into (26), which is itself substituted into (24) to give the direct evaporation rate and into (25) to give the transpiration rate.

Ground temperatures in the model are calculated by substituting (9)-(11) into (8), linearizing the result, and iteratively solving the resulting energy balance equation,

$$T_{g,c,t,n} = T_{g,c,t,n-1} + \frac{\left\{ \begin{array}{l} -f_{s,c}\dfrac{\overline{\rho}_a c_{p,d}}{R_{a,c}}\left[\overline{\theta}_p(z_r) - \dfrac{T_{g,c,t,n-1}}{\overline{P}_g}\right] \\ -f_{v,c}\dfrac{\overline{\rho}_a c_{p,d}}{R_{f,c}}\left[\dfrac{T_{af,c,t}}{\overline{P}_f} - \dfrac{T_{g,c,t,n-1}}{\overline{P}_g}\right] \\ -f_{s,c}\dfrac{\overline{\rho}_a L_e}{R_{a,c}}\beta_{g,c}\left[\overline{q}_v(z_r) - q_{v,s}\left(T_{g,c,t-h}\right)\right] \\ -f_{v,c}\dfrac{\overline{\rho}_a L_e}{R_{f,c}}\beta_{g,c}\left[q_{af,c} - q_{v,s}\left(T_{g,c,t-h}\right)\right] \\ -f_{s,c}\overline{F}_s - \overline{F}_i - \sigma_B\left(\overline{\varepsilon}\overline{T}^4_{g,t-h} - \varepsilon_{s,c}T^4_{g,c,t,n-1}\right) \\ -\dfrac{\kappa_{s,1,c}}{D_1}\left(T_{1,c,t} - T_{g,c,t,n-1}\right) \end{array} \right\}}{-f_{s,c}\dfrac{\overline{\rho}_a c_{p,d}}{R_{a,c}\overline{P}_g} - f_{v,c}\dfrac{\overline{\rho}_a c_{p,d}}{R_{f,c}\overline{P}_g} - 4\varepsilon_{s,c}\sigma_B T^3_{g,c,t,n-1} - \dfrac{\kappa_{s,1,c}}{D_1}}. \quad (32)$$

where D_1 (m) is the positive distance between the surface and the middle of the first soil layer, and $T_{1,c,t}$ (K) is the temperature at the middle of the top soil layer, predicted with the solution to (2). Equation (32) is iterated four times for each surface class without updating the saturation mixing ratio in the soil during each iteration. Finally, the grid-cell-averaged fluxes of sensible heat (J m^{-2} s^{-1}) and moisture (kg m^{-2} s^{-1}) to the boundary layer are

$$\overline{H}_f = \sum_c f_c\left(H_{g,c} + H_{v,c}\right), \quad (33)$$

$$\overline{E}_f = \sum_c f_c\left(E_{g,c} + E_{d,c} + E_{t,c}\right), \quad (34)$$

respectively (positive is up in both cases), where the individual fluxes for each soil class are calculated with updated values of ground and foliage temperatures.

3.3. Road and Rooftop Surfaces

Construction materials, such as asphalt, concrete, wood, brick, and composites cover a sufficient portion of metropolitan areas that such surfaces should be treated differently from soil surfaces. Ideally, each surface would be treated separately by considering sensible, latent, and radiative heat fluxes to the surface and heat conduction through the surfaces. The problem with such treatment is that so many compositions exist, and material compositions change significantly over short distances. Here, urban and built-up land surfaces are treated by assuming they consist of roads (and other impervious ground surfaces), rooftops, vegetation, and bare soil. Since vegetation and bare soil are separated out of the urban portion of each grid cell, only road and rooftop surfaces are discussed here. Another important component of the energy balance in urban regions is wall surfaces. Wall surfaces are ignored for the present study due to the additional complexity involved in treating the nonhorizontal nature of these surfaces.

Oke [1999] found that 25% of surfaces affecting the energy balance in a densely built-up central Mexico City site consisted of impervious ground materials, 32% consisted of rooftops, 42% consisted of walls, and 1% consisted of vegetation. A similar Vancouver site consisted of 32% impervious ground materials, 37% rooftops, 27% walls, and 4% vegetation. These two studies indicate that the ratio of rooftop to impervious ground material surfaces was about 1.22 to 1. This ratio is used for the present study. The fraction of vegetation in urban/built-up regions varies widely. While the above studies reported low vegetation fractions, other studies cited by *Oke* [1999] reported vegetation fractions of 94% for a rural site, 70% for an urban residential site, and 16% for an urban commercial site. To account for this wide range of possible vegetation fractions, it is assumed that an average of 40% of all 1 x 1 km urban and built-up land cover/land use cells are covered by vegetation and 10% are covered by bare soil. The remainder of each cells is assumed to consist of impervious ground material (22.5% of total area) and rooftops (27.5% of total area).

Temperatures of impervious ground material are calculated by first assuming that such material consists primarily of asphalt (although concrete is another important material overlying the ground). It is assumed that an average asphalt layer is about 6 cm thick and that it overlies the dominant soil class in the grid cell. When the 10-layer soil model is applied to this configuration, the top five layers are asphalt, and the remaining layers, extending down to 0.5 m, are soil containing liquid water. The asphalt is assumed to be impermeable to water, and the heat conduction equation is solved assuming a mean thermal conductivity of various asphalts of κ_{as}=1.7 W m^{-1} K^{-1} [*Anandakumar*, 1999] and a thermal conductivity of an air-soil-water mixture below.

At the ground, an equilibrium energy balance equation that accounts for sensible heat, latent heat, radiative, and conductive heat fluxes is iterated four times to calculate final ground temperature after a time step (s) h. Although the asphalt is impermeable to liquid water, water can condense onto, precipitate onto, or evaporate from the surface. Snow can fall on or sublimate from the surface as well. Snow cover is treated in section 3.4. The predicted temperature over non-snow-covered asphalt after a time step is calculated as

$$T_{g,c,t,n} = T_{g,c,t,n-1} + \frac{\left\{ \begin{array}{l} -\dfrac{\overline{\rho}_a c_{p,d}}{R_{a,c}}\left[\overline{\theta}_p(z_r) - \dfrac{T_{g,c,t,n-1}}{\overline{P}_g}\right] \\ -\dfrac{\overline{\rho}_a L_e}{R_{a,c}}\beta_d\left[\overline{q}_v(z_r) - q_{v,s}\left(T_{g,c,t-h}\right)\right] \\ -\overline{F}_s - \overline{F}_i - \sigma_B\left(\overline{\varepsilon}\overline{T}^4_{g,t-h} - \varepsilon_{as}T^4_{g,c,t,n-1}\right) \\ -\dfrac{\kappa_{as}}{D_1}\left(T_{1,c,t} - T_{g,c,t,n-1}\right) \end{array} \right\}}{-\dfrac{\overline{\rho}_a c_{p,d}}{R_{a,c}\overline{P}_g} - 4\varepsilon_{as}\sigma_B T^3_{g,c,t,n-1} - \dfrac{\kappa_{as}}{D_1}} \quad (35)$$

where ε_{as}=0.95 is the thermal-IR emissivity of asphalt [*Oke*, 1978], D_1 (m) is the distance between the ground surface and the middle of first asphalt layer, and β_d is the function from (26), which requires the calculation of W_c from (31). Here, W_c accounts for condensation/evaporation and precipitation/runoff over the asphalt surface. When precipitation or condensation (dew formation) occurs, all liquid water above $W_{\max,c}$ is runoff, and the liquid water below $W_{\max,c}$ is allowed to evaporate.

Many types of roofing exist, and rooftop types generally differ between residential and commercial buildings. Throughout the United States, four out of five residential

rooftops contain asphalt shingles. Asphalt-shingle roof systems consist of asphalt shingles overlying saturated felt, overlying a water-impermeable membrane, overlying a roof deck, overlying insulation or air. Asphalt shingles are either organic or fiberglass based. Organic-based shingles contain a base of cellulose fibers, which is saturated with an asphalt coating and surfaced with weather-resistant mineral granules. Fiberglass-based shingles contain a base of glass fibers surfaced with an asphalt coating and weather-resistant mineral granules. The saturated felt is an asphalt-impregnated, organic-based felt between the roofing material and the waterproof membrane [*Asphalt Roofing Manufacturers Association*, 1999]. Other residential rooftops consist of wood shake, concrete tiles, or slate over a membrane over a deck and insulation over air.

Many commercial rooftops also consist of asphalt shingles, but others consist of two to four layers of bitumen strengthened with a fabric, such as polyester or fiberglass, or with a felt. Gravel or granules are usually embedded on the top layer of strengthened bitumen. The bitumen layers usually overlie insulation, a vapor retarder, and a deck. Bitumen is a black or dark-colored cement-like, solid, semi-solid, or viscous substances composed of high-molecular-weight hydrocarbons and found in asphalts, tars, pitches, and asphaltines.

Since asphalt shingles are the most common residential rooftop and possibly the most common rooftop in the United States, it is assumed that they are the most representative. It is assumed that the average rooftop consists of 1.5-cm-thick asphalt shingles over a 1.0-cm-thick saturated felt (asphalt-felt composite) over a 1.25-cm-thick plywood base over air. This configuration is fitted into the 10-layer surface module by assuming that asphalt shingles and saturated felt have thermal conductivities and specific heats similar to those of asphalt. It is assumed that no liquid water passes through a roof, but it can condense or precipitate onto the roof. Snow can also deposit on the roof. When the 10-layer subsurface module is applied to a rooftop, (35) is used to calculate rooftop temperatures.

3.4. Snow on Soil, Vegetation, and Asphalt

When snow falls or preexists, the snow surface temperature is calculated iteratively with (32) for soil/vegetation surfaces and (35) for road/soil and rooftop/air surfaces with modification. The thickness of each layer of the 10-layer subsurface module stays the same, but the module as a whole moves upward when snow accumulates and downward when snow melts, so that the top of the module is always at the air-surface interface. Thus, the number of subsurface snow layers depends on the snow depth. If any snow is present, the top layer, 0.005 m thick, is assumed to consist entirely of snow.

Ground and direct turbulent moisture fluxes from snow over soil and vegetation are calculated with (11) and (25), respectively, except that in the equations, $\beta_{g,c}$ is set to unity, $q_{v,s}\left(T_{f,c}\right)$ (kg kg^{-1}) is defined as the saturation mixing ratio over ice, not liquid water, and L_e is replaced with L_s, the latent heat of sublimation (J kg^{-1}). The sensible heat fluxes across soil and vegetation, given by (10) and (23), respectively, are not changed. In (23) and (33), the emissivity of snow is set to $\varepsilon_{s,c} = \varepsilon_{v,c} = \varepsilon_{sn}$=0.99 and the thermal conductivity of snow is set to $\kappa_{s,1,c} = \kappa_{sn}$=0.08 W m^{-1} K^{-1} [*Oke*, 1978]. For snow on top of vegetation, transpiration through leaf surfaces is set to zero ($E_{t,c}$=0). For snow on top of asphalt road surfaces or asphalt shingle rooftops, ε_{as}, κ_{as}, and L_e in (35) are replaced by ε_{sn}, κ_{sn}, and L_s, respectively, β_d is set to unity, and $q_{v,s}\left(T_{g,c,t-h}\right)$ (kg kg^{-1}) is defined as the saturation mass mixing ratio over ice rather than liquid water.

Snow depth D_s is initialized with a monthly-averaged 1° x 1° global data set [*NASA*, 1992]. The depth is predicted in time by accounting for snowfall and melting. Rain in the model is converted to snowfall when the ground air temperature $\le T_{s,m}$. In such a case, the grid-cell-averaged snowfall (m s^{-1}) rate is calculated as $\overline{P}_s = \overline{P}_r \rho_s / \rho_w$, where ρ_{sn}=100 kg m^{-3} [*Oke*, 1978] is the density of fresh snow. When snow preexists, and the snow temperature, predicted by (32) $\le T_{s,m}$, no melting is considered and the new snow depth is calculated as $D_{s,t} = D_{s,t-h} + h\overline{P}_s$. When the predicted snow temperature exceeds $T_{s,m}$, melting occurs from the top, the snow temperature is set to $T_{s,m}$, and the snow depth over asphalt/soil surfaces (where $f_{s,c}$=1 and $f_{v,c}$=0) or vegetation/soil surfaces is recalculated as

$$D_{s,t} = D_{s,t-h} + h\overline{P}_s + h\times \frac{\left\{\begin{array}{l} -f_{s,c}\dfrac{\overline{\rho}_a c_{p,d}}{R_{a,c}}\left[\overline{\theta}_p(z_r) - \dfrac{T_{s,m}}{\overline{P}_g}\right] - f_{v,c}\dfrac{\overline{\rho}_a c_{p,d}}{R_{f,c}}\left[\dfrac{T_{af,c,t}}{\overline{P}_f} - \dfrac{T_{s,m}}{\overline{P}_g}\right] \\ -f_{s,c}\dfrac{\overline{\rho}_a L_s}{R_{a,c}}\left[\overline{q}_v(z_r) - q_{v,s}\left(T_{s,m}\right)\right] - f_{v,c}\dfrac{\overline{\rho}_a L_s}{R_{f,c}}\left[q_{af,c} - q_{v,s}\left(T_{s,m}\right)\right] \\ -f_{s,c}\overline{F}_s - \overline{F}_i - \sigma_B\left(\overline{\varepsilon}\overline{T}_{g,t-h}^4 - \varepsilon_{sn}T_{s,m}^4\right) - \dfrac{\kappa_{sn}}{D_1}\left(T_{1,c,t} - T_{s,m}\right) \end{array}\right\}}{\rho_{sn} L_m} \quad (36)$$

where L_m is the latent heat of melting (J kg^{-1}), and $q_{v,s}\left(T_{s,m}\right)$ is the saturation mass mixing ratio (kg kg^{-1}) over ice at the melting point of snow. Equation (36) assumes that all snow on vegetation (except a small amount sticking to leaf surfaces) falls to the ground.

3.5. Water, Sea Ice, and Snow-Covered Sea Ice

Over oceans, inland seas, and lakes, the water-top temperature is predicted with

$$T_{g,c,t} = T_{g,c,t-h} + h\frac{\left\{\begin{array}{l} -\dfrac{\overline{\rho}_a c_{p,d}}{R_{a,c}}\left[\overline{\theta}_p(z_r) - \dfrac{T_{g,c,t-h}}{\overline{P}_g}\right] \\ -\dfrac{\overline{\rho}_a L_e}{R_{a,c}}\left[\overline{q}_v(z_r) - q_{v,s}\left(T_{g,c,t-h}\right)\right] \\ -\overline{F}_s - \overline{F}_i - \sigma_B\left(\overline{\varepsilon}\overline{T}_{g,t-h}^4 - \varepsilon_w T_{g,c,t-h}^4\right) \end{array}\right\}}{\rho_{sw} c_{p,sw} D_l}, \quad (37)$$

where $q_{v,s}\left(T_{g,c,t-h}\right)$ (kg kg^{-1}) is the saturation mass mixing ratio over liquid water at the temperature of the water, ε_w=0.97 is the thermal-IR emissivity of liquid water [*Oke*, 1978], ρ_{sw} is the density of seawater (1028 kg m^{-3} at 0 °C in the presence of 35 parts per 1000 of salinity [*Lide*, 1998]), $c_{p,w}$ is the temperature-dependent specific heat of liquid water at constant pressure (3986.5 J kg^{-1} K^{-1} at 0°C in the presence of 35 parts per 1000 of salinity), and D_l=30 m is the assumed depth of ocean water in which energy and salinity are well mixed [*Parkinson and Washington*, 1979]. Initial sea surface

temperatures are obtained from the Fleet Numerical Meteorology and Oceanography Center.

When the water temperature predicted by (37) falls below $T_{i,f}$=271.23 K, the freezing point of seawater in the presence 35 parts per 1000 of salinity [*Lide*, 1998], a layer D_i = 0.01 m thick of ice is assumed to form. The ice surface temperature is then determined with the four-iteration equilibrium calculation,

$$T_{g,c,t,n} = T_{g,c,t,n-1} + \frac{\left\{\begin{array}{l} -\frac{\overline{\rho}_a c_{p,d}}{R_{a,c}}\left[\overline{\theta}_p(z_r) - \frac{T_{g,c,t,n-1}}{\overline{P}_g}\right] \\ -\frac{\overline{\rho}_a L_s}{R_{a,c}}\left[\overline{q}_v(z_r) - q_{v,s}\left(T_{g,c,t-h}\right)\right] \\ -\overline{F}_s - \overline{F}_i - \sigma_B\left(\overline{\varepsilon}\overline{T}^4_{g,t-h} - \varepsilon_i T^4_{g,c,t,n-1}\right) \\ -\frac{\kappa_i}{D_{i,t-h}}\left(T_{i,f} - T_{g,c,t,n-1}\right) \end{array}\right\}}{-\frac{\overline{\rho}_a c_{p,d}}{R_{a,c}\overline{P}_g} - 4\varepsilon_i T^3_{g,c,t,n-1} - \frac{\kappa_i}{D_{i,t-h}}}, \quad (38)$$

where $q_{v,s}\left(T_{g,c,t-h}\right)$ is the saturation mixing ratio over ice, ε_i=0.97 is the thermal-IR emissivity of ice [*Parkinson and Washington*, 1979], and κ_i=2.20 W m^{-1} K^{-1} is the thermal conductivity of ice [*Lide*, 1998]. If the ice temperature predicted by (38) exceeds $T_{i,m}$=273.05 K, the melting point of ice, the ice-surface temperature is set to $T_{i,m}$ and the change in ice thickness due to melting at the top is

$$D_{i,t} = D_{i,t-h} + h\frac{\left\{\begin{array}{l} -\frac{\overline{\rho}_a c_{p,d}}{R_{a,c}}\left[\overline{\theta}_p(z_r) - \frac{T_{i,m}}{\overline{P}_g}\right] \\ -\frac{\overline{\rho}_a L_s}{R_{a,c}}\left[\overline{q}_v(z_r) - q_{v,s}\left(T_{i,m}\right)\right] \\ -\overline{F}_s - \overline{F}_i - \sigma_B\left(\overline{\varepsilon}\overline{T}^4_{g,t-h} - \varepsilon_i T^4_{i,m}\right) \\ -\frac{\kappa_i}{D_{i,t-h}}\left(T_{i,f} - T_{i,m}\right) \end{array}\right\}}{\rho_i L_m}, \quad (39)$$

where ρ_i (kg m^{-3}) is the density of ice (916.7 kg m^{-3} at 273.05 K). When the temperature of ice predicted by (38) is below $T_{i,m}$, no change in thickness at the top occurs. A change in thickness at the water-ice interface continuously occurs and is calculated as

$$D_{i,t} = D_{i,t-h} + h\left\{\frac{\overline{F}_b - \frac{\kappa_i}{D_{i,t-h}}\left(T_{i,f} - T_{g,c,t}\right)}{\rho_i L_m}\right\}, \quad (40)$$

where $\overline{F}_b$ (W m^{-2}) is the net flux of energy from below the interface, assumed to be 2 W m^{-2} for Arctic waters and 25 W m^{-2} for Antarctic waters, and the second term accounts for conduction between the interface and the top of the ice [*Parkinson and Washington*, 1979]. Maximum ice thickness are typically 4 m in the Arctic and 1.5 m in the Antarctic.

When sea ice exists and snowfall occurs, the snow is assumed to coat the ice. The temperature at the top of the snow is predicted with

$$T_{g,c,t,n} = T_{g,c,t,n-1} + \frac{\left\{\begin{array}{l} -\frac{\overline{\rho}_a c_{p,d}}{R_{a,c}}\left[\overline{\theta}_p(z_r) - \frac{T_{g,c,t,n-1}}{\overline{P}_g}\right] \\ -\frac{\overline{\rho}_a L_s}{R_{a,c}}\left[\overline{q}_v(z_r) - q_{v,s}\left(T_{g,c,t-h}\right)\right] \\ -\overline{F}_s - \overline{F}_i - \sigma_B\left(\overline{\varepsilon}\overline{T}^4_{g,t-h} - \varepsilon_{sn} T^4_{g,c,t,n-1}\right) \\ -\frac{\kappa_{sn}\kappa_i}{\kappa_{sn}D_{i,t-h} + \kappa_i D_{s,t-h}}\left(T_{i,f} - T_{g,c,t,n-1}\right) \end{array}\right\}}{-\frac{\overline{\rho}_a c_{p,d}}{R_{a,c}\overline{P}_g} - 4\varepsilon_{sn} T^3_{g,c,t,n-1} - \frac{\kappa_{sn}\kappa_i}{\kappa_{sn}D_{i,t-h} + \kappa_i D_{s,t-h}}}, \quad (41)$$

where the thermal conductivity term accounts for conduction through ice and snow layers. The temperature at the snow-ice interface is [*Parkinson and Washington*, 1979]

$$T_I = \frac{\kappa_{sn}D_{i,t-h}T_{g,c,t} + \kappa_i D_{s,t-h}T_{i,f}}{\kappa_{sn}D_{i,t-h} + \kappa_i D_{s,t-h}}. \quad (42)$$

If the temperature predicted by (41) exceeds the melting point of snow, $T_{s,m}$, the change in snow thickness on top of the ice is calculated with (36), except that T_I from (42) is substituted for $T_{1,c,t}$. Melting from the bottom of the ice layer when snow is present is still calculated with (40).

3.6. Analysis of Ground Surface Predictions

Here, predictions of several temperature parameters from an August 1990 northern California simulation (where grid spacing was 0.05° x 0.05°) are analyzed, and the resulting air temperatures are compared with data. Details of the model simulations, data used, and additional comparisons of temperature predictions with data are given in *Jacobson* [this issue].

Figure 2a shows time series predictions of foliage air temperature ($T_{af,c}$), foliage temperature ($T_{f,c}$), ground temperature ($T_{g,c}$), and above-canopy air temperature ($\overline{T}_a$, taken at the midlevel of the bottom model layer) over sandy loam in a grid cell containing the Lodi (LOD) temperature monitoring site. The Lodi site is rural and located in the San Joaquin Valley [*Jacobson*, this issue, Figure 2]. Figure 2a here indicates that during the day, foliage temperatures exceeded foliage air temperatures, which exceeded ground temperatures, which exceeded air temperatures. The Lodi cell contains about 58.4% sandy loam and 41.6% clay loam. Figure 2b shows the modeled differences in temperatures between sandy loam and clay loam in the cell. Above-canopy air temperatures above both soil classes are the same in the model. The figure shows that differences in ground temperatures over the two soil types were up to 10°C during the day. The differences are most likely due to the large differences in soil parameters between sandy loam and clay loam. The large difference implies that representation of this grid cell by one but not both of the soil classes will cause differences in predicted air temperatures.

Figure 2c shows predicted and observed air temperatures at Lodi when both soil types were retained for the cell. The predictions were obtained from bilinear interpolation of air temperatures from four adjacent grid cells to the vertical center of the bottom model layer at the Lodi site, then interpolated vertically to the observation altitude, estimated at 5 m, an average height for temperature measurements in northern California.

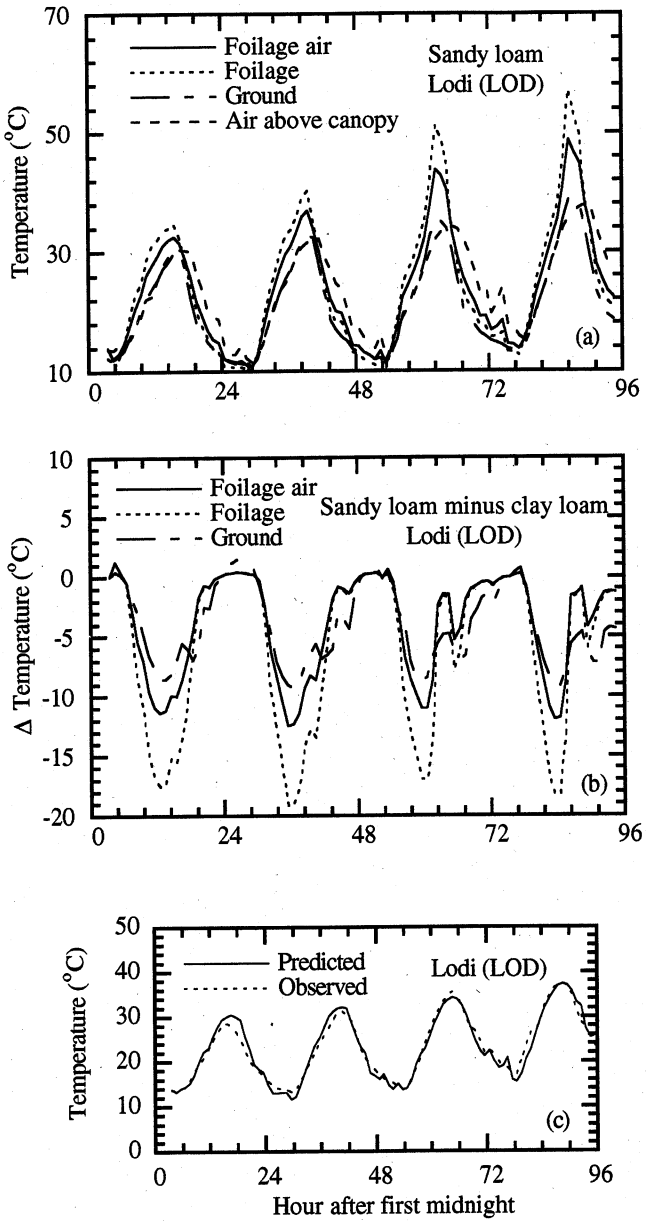

Figure 2. (a) Time series plot of predicted foliage air temperature (T_{af}) foliage temperature (T_f), ground temperature (T_g), and air temperature above the canopy (T_a) over clay soil in a grid cell of the NCal domain containing the Lodi (LOD) monitoring site. (b) Difference between temperatures over clay and those over clay loam in the same grid cell. (c) Predicted air temperatures at 5 m versus observations at the Lodi monitoring site. The predicted values were obtained from bilinear interpolation of modeled air and ground temperatures at four grid cells to the Lodi site. Air and ground temperatures were then interpolated vertically to the observation altitude.

Figure 3 shows results similar to Figure 2, but for a suburban site, Fremont, whose surfaces were estimated to consist of 40% silt loam, 26.2% silt clay loam, 13.4% roof, 11.4% clay, 8.9% road, and 0.001% loam. Fremont is just to the east of the San Francisco Bay; thus, its diurnal temperature variations are weaker than those at Lodi. Figure 3a shows predicted temperatures over clay, and Figures 3b-3d show differences between the temperatures over clay and those over other soils. The differences in temperatures over different soils at Fremont were smaller than those at Lodi, due primarily to smaller differences in soil parameters among the soil types at Fremont.

Figure 3e shows predicted soil, road, and roof temperatures at Fremont. Roads were the hottest surfaces during the day, since asphalt contains no water, and energy conduction to soil below asphalt is slow. Peak temperatures over asphalt varied from 43° to 52°C. *Anandakumar* [1999] shows a peak August temperature over an asphalt road at Vienna, Austria, 10° latitude farther north than Fremont, of 44°C. Rooftop temperatures here were cooler than road temperatures, because air under a rooftop convects away energy conducted to it by the roof faster than soil conducts away energy conducted to it by asphalt.

4. Minimization of Memory During Nesting

An important feature of the one-way-nested model is that memory requirements are minimized so that total required central memory never exceeds about 1.5 times the central memory of the largest model domain for gas simulations and 2.1 times the central memory of the largest domain for gas/aerosol simulations. Thus, if the largest domain requires 53 megawords (0.4 GB) of central memory and ten nested domains are used, the total central memory of the model increases to only 80 megawords (0.64 GB) for gas simulations. In the absence of array savings the central memory requirement would increase to about 500 megawords (4 GB), beyond the central memory capacity of most computers.

Memory savings are obtained by solving one domain at a time over a specified time interval (e.g., 30 min.), writing information from the domain to hard disk at the end of the interval, and reusing the same arrays for all variables in all subsequent domains. The first domain solved is the global domain. At the end of a nesting time interval, all arrays for restarting the global computation and for providing boundary conditions for domains in the next layer of nesting are written to hard disk. Each domain in the next layer of nesting is then solved, one at a time. Such domains read in boundary-condition information from their "parent" domain. After each domain is solved, arrays from it are written to hard disk. Subsequent layers of nesting are solved in a similar manner.

Once the last domain in the last layer is solved, the global domain reads in arrays stored from the last time interval, and the next time-interval is solved. When the interval is finished, arrays are written again to disk, overriding the arrays from the previous interval. Since all domains in the model reuse the same arrays and carry the same variables, the total memory required for the model as a whole is limited only by the domain with the largest number of grid cells. There is no requirement as to which domain has the largest number of grid cells, and there is no requirement as to how many grid cells a given domain can have (except that total memory for the domain with the largest number of grid cells is limited by the memory available on the computer).

The use of this technique requires a fixed amount of hard disk space for each domain, regardless of the time interval or length of simulation. The information from a domain stored on disk includes all arrays from the end of the most recent time interval. For 100 domains in which 1 GB each of array information is stored, 100 GB total of hard disk space is needed. Currently, the total cost of disk storage for 100 GB is less than $6,000.

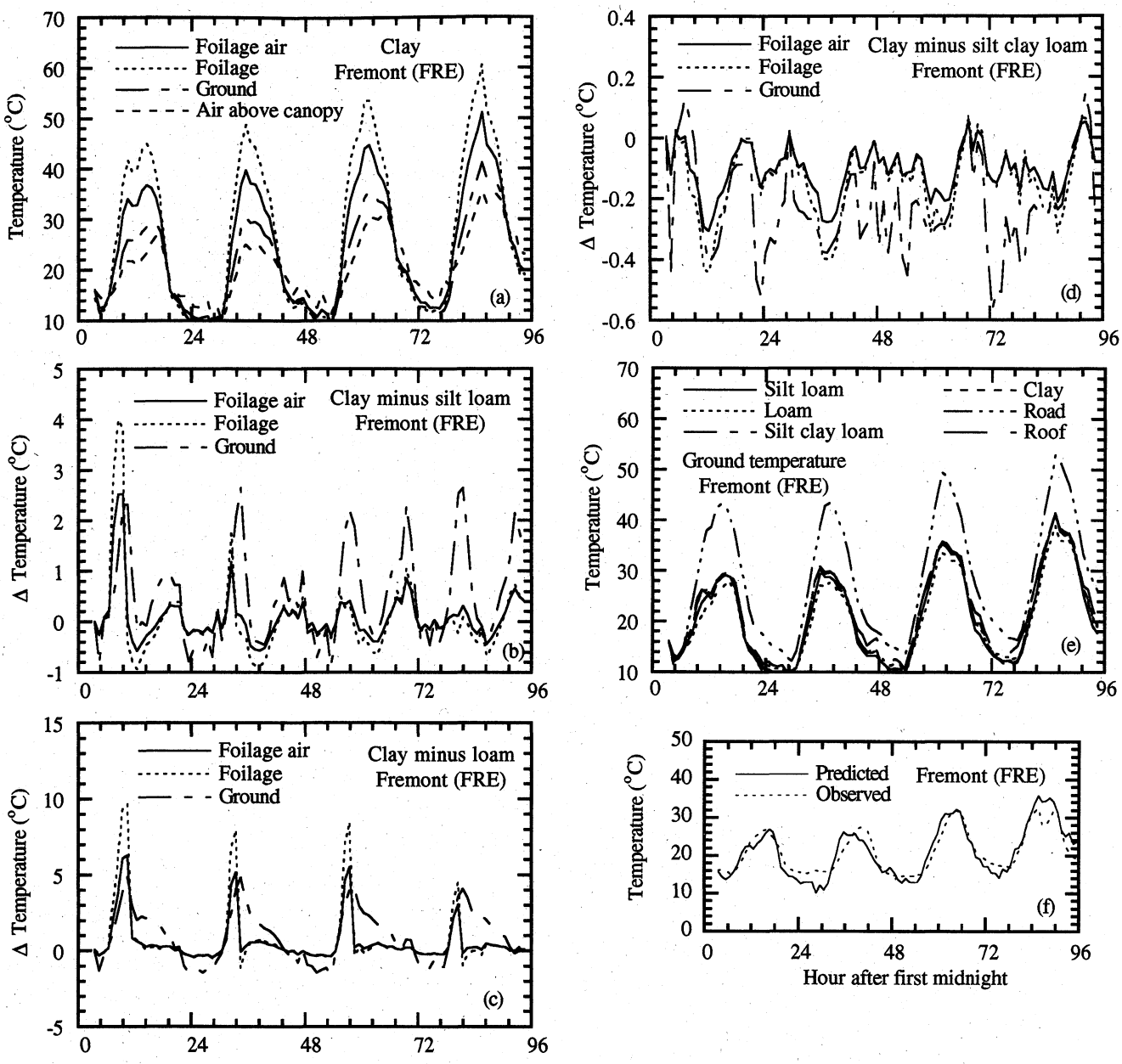

Figure 3. (a) Same as Figure 2a, except for clay soil at the Fremont (FRE) monitoring site. (b-d) Same as Figure 2b, except for clay minus silt loam, clay minus loam, and clay minus silt clay loam at Fremont. (e) Predicted ground temperatures over four soil types, road surfaces, and rooftops at Fremont. (f) Same as Figure 2c, except at Fremont.

The storage technique above permits two-way and one-way nesting, but two-way nesting is avoided here, because such nesting results in perturbations to velocities, potential temperature, etc., in the middle of the coarse domain that degrade the energy/potential enstrophy (global scale) and energy/enstrophy (regional) conservation properties of the numerical solutions to the momentum and thermodynamic energy equations used here. Numerical schemes in meteorological models that do not conserve these parameters (e.g., those that perform central differencing to high order across a cell) may not be concerned with this issue although two-way nesting may erode other properties of such models. In one comparison of a storm prediction with observations with the MM5 model, one-way nesting produced domain-averaged precipitation, a 500-mbar trough, and the location of maximum precipitation as well as or better than the two-way nesting [*Lozej and Bornstein,* 1999].

GATOR-GCMM can be implemented on a parallel computer in at least two ways. The first is to solve all domains sequentially but to parse out sections of each domain to different processors. Since chemical, radiative, aerosol, and transport solution processes are already divided into grid blocks, columns, or rows, such parsing is straightforward for these processes. A second method is to put different domains on different processors. This requires solving "parent" domains one or more time intervals ahead of finer domains, since solutions from parent domains are needed to provide boundary values for finer domains.

5. Computer Time Requirements

The computer time required to solve gas chemistry (115 gases, 220 reactions), meteorology, radiative transfer (409 wavelengths), species transport (115 gases), ground temperature calculations, and input/output with GATOR-GCMM over an average domain size of 100,000 cells on an SGI Origin 2000 was about 53 min per hour of simulation per domain. The use of five domains this size required about 4.4 days of computer time per day of simulation on a single processor (or 21 hours per domain per day). Of the computer time, about 32 s per hour of simulation per domain (<1% of total computer time) was required for writing to plus reading from disk. Thus, the memory-minimization technique described here uses minimal computer time. On a Compaq 21264 (667 MHz) 64-MB chip, the speed is approximately three times faster than on an SGI Origin 2000, reducing computer time of a five-domain model on a single processor to 1.5 days per day of simulation (or 7 hours per day per domain per processor).

6. Conclusion

A global- through urban-scale air pollution/weather forecast model was developed. The model treats nesting of all important air quality and meteorological parameters in each domain, any number of nested layers, and any number of domains in each layer. The central memory requirement of the model as a whole never exceeds 1.5 (2.1) times the central memory requirement of the largest domain when gas (gas/aerosol) processes are solved. The model treats ground temperature, latent heat fluxes, and sensible heat fluxes over subgrid soil and vegetation covers. The module also treats temperatures and fluxes over water, sea ice, snow-covered sea ice, and urban areas. Urban areas are divided into road surfaces, rooftops, vegetation, and bare soil. A high-resolution global soil texture classification data set was derived from an existing 1 km x 1 km high-resolution U.S. texture classification data set and from a 10 km x 10 km soil-type data set. The soil texture data set was coupled with 1 km x 1 km land use/land cover data to define subgrid soil texture classes, vegetation fractions, and urban land cover. The GATOR-GCMM model is applied to an air pollution case study in part 2 of this work.

Acknowledgments. This work was supported, in part, by grants from the National Science Foundation under agreements ATM-9504481 and ATM-9614118, the National Aeronautics and Space Administration under the New Investigator Program (NIP) in Earth Sciences, and the David and Lucile Packard Foundation and the Hewlett-Packard company through a Stanford University Terman Fellowship. I would also like to thank Phil Martien of the Bay Area Air Quality Management District for providing certain SARMAP data fields, Jinyou Liang of Stanford University and Roberto San Jose from the Technical University of Madrid for help in facilitating the use of large data sets, and Afshin Tabazadeh of Best Roofing Co. for providing information about rooftop composition.

References

Anandakumar, K., A study of the partition of net radiation into heat fluxes on a dry asphalt surface, *Atmos. Environ.*, *33*, 3911-3918, 1999.

Anthes, R. A., E. Y. Hsie, and Y. H. Kuo, Description of the Penn State/NCAR Mesoscale Model Version 4 (MM4), *NCAR Tech. Note, NCAR/TN-282+STR*, Natl. Cent. for Atmos. Res., Boulder, Colo., 1987.

Arakawa, A., *Boundary Conditions in Limited-Area Models*, Course notes, Dep. of Atmos. Sci., Univ. of Calif., Los Angeles, 1982.

Arakawa, A., *Introduction to the UCLA General Circulation Model*, Course Notes, Univ. of Calif., Los Angeles, 1995.

Arakawa, A., and V. R. Lamb, Computational design of the basic dynamical processes of the UCLA general circulation model, *Meth. Comput. Phys.*, *17*, 174-265, 1977.

Arakawa, A., and V. R. Lamb, A potential enstrophy and energy conserving scheme for the shallow water equations, *Mon. Weather Rev.*, *109*, 18-36, 1981.

Arakawa, A., and W. H. Schubert, Interaction of a cumulus cloud ensemble with large scale environment, part I, *J. Atmos. Sci.*, *31*, 674-701, 1974.

Arakawa, A., and M. J. Suarez, Vertical differencing of the primitive equations in sigma coordinates, *Mon. Weather Rev.*, *111*, 34-45, 1983.

Asphalt Roofing Manufacturers Association (ARMA), *Roofing Basics*, http://www.asphaltroofing.org/basics.html, 1999.

Baldocchi, D. D., B. B. Hicks, and P. Camara, A canopy stomatal resistance model for gaseous deposition to vegetated surfaces, *Atmos. Environ.*, *21*, 91-101, 1987.

Binkowski, F. S., and U. Shankar, The regional particulate matter model, 1, Model description and preliminary results, *J. Geophys. Res.*, *100*, 26,191-26,209, 1995.

Blackadar, A. K., Modeling the nocturnal boundary layer, in *Preprints of Third Symposium on Atmospheric Turbulence, Diffusion, and Air Quality*, Am. Meteorol. Soc., Boston, Mass., 1976.

Briggs, G. A., Plume rise predictions, chap. 3 in *Lectures on Air Pollution and Environmental Impact Analyses*, Am. Meteorol. Soc., Boston, Mass., 1975.

Businger, J. A., J. C. Wyngaard, Y. Izumi, and E. F. Bradley, Flux-profile relationships in the atmospheric surface layer, *J. Atmos. Sci.*, *28*, 181-189, 1971.

Byun, D. W., and J. K. S. Ching (Eds.), *Science Algorithms of the EPA Models-3 Community Multiscale Air Quality (CMAQ) Modeling System, EPA/600/R-99/030*, U.S. Environ. Prot. Agency, Off. of Res. and Dev., Washington, D. C., 1999.

Clapp, R. B., and G. M. Hornberger, Empirical equations for some soil hydraulic properties, *Water Resour. Res.*, *14*, 601-604, 1978.

Copeland, J. H., R. A. Pielke, and T. G. F. Kittel, Potential climatic impacts of vegetation change: A regional modeling study, *J. Geophys. Res.*, *101*, 7409-7418, 1996.

Damassa, J., S. Tanrikulu, K. Magliano, A. J. Ranzieri, and E. Niccum, Performance evaluation of SAQM in central California and attainment demonstration for the 3-6 August 1990 ozone episode, Calif. Air Resour. Board, Sacramento, 1996.

Deardorff, J. W., Efficient prediction of ground surface temperature and moisture with inclusion of a layer of vegetation, *J. Geophys. Res.*, *83*, 1889-1903, 1978.

Dickinson, R. E., Modeling evapotranspiration for three-dimensional global climate models, in *Climate Processes and Climate Sensitivity, Geophys. Monogr. Ser.*, vol. 29, edited by J. E. Hanson and T. Takahashi, pp. 58-72, 1984.

Dickinson, R. E., R. M. Errico, F. Giorgi, and G. T. Bates, A regional climate model for the western United States, *Clim. Change*, *15*, 383-422, 1989.

Ding, P., and D. A. Randall, A cumulus parameterization with multiple cloud-base levels, *J. Geophys. Res.*, *103*, 11,341-11,353, 1998.

Dolman, A. J., and E. M. Blyth, Patch scale aggregation of heterogeneous land surface cover for mesoscale meteorological models, *J. Hydrol.*, *190*, 252-263, 1997.

Dudek, M.-P., X.-Z. Liang, and W.-C. Wang, A regional climate model study of the scale-dependence cloud-radiation interaction, *J. Clim.*, *9*, 1221-1234, 1996.

Food and Agricultural Organization (FAO), *Soil Map of the World*, Land and Water Dev. Div., Rome, Italy, 1995.

Giorgi, F., and G. T. Bates, On the climatological skill of a regional model over complex terrain, *Mon. Weather Rev.*, *117*, 2325-2347, 1989.

Giorgi, F., and M. R. Marinucci, Improvements in the simulation of surface climatology over the European region with a nested modeling system, *Geophys. Res. Lett.*, *23*, 273-276, 1996.

Giorgi, F., and L. O. Mearns, Introduction to special section: Regional climate modeling revisited, *J. Geophys. Res.*, *104*, 6335-6352, 1999.

Grell, G. A., J. Dudhia, and D. R. Stauffer, Description of the fifth-generation Penn State/NCAR mesoscale model (MM5), *NCAR Tech. Note, NCAR/TN-398+STR*, 117 pp., Natl. Cent. for Atmos. Res., Boulder, Colo., 1994.

Hogstrom, U., Nondimensional wind and temperature profiles in the

atmospheric surface layer: A reevaluation. *Boundary Layer Meteorol., 42*, 55-78, 1988.

Jacobson, M. Z., Computation of global photochemistry with SMVGEAR II, *Atmos. Environ., 29(A)*, 2541-2546, 1995.

Jacobson, M. Z., Development and application of a new air pollution modeling system, part II, Aerosol module structure and design, *Atmos. Environ., 31*, 131-144, 1997a.

Jacobson, M. Z., Development and application of a new air pollution modeling system, part III, Aerosol-phase simulations, *Atmos. Environ., 31*, 587-608, 1997b.

Jacobson, M. Z., Studying the effects of aerosols on vertical photolysis rate coefficient and temperature profiles over an urban airshed, *J. Geophys. Res., 103*, 10,593-10,604, 1998a.

Jacobson, M. Z., Improvement of SMVGEAR II on vector and scalar machines through absolute error tolerance control, *Atmos. Environ., 32*, 791-796, 1998b.

Jacobson, M. Z., *Fundamentals of Atmospheric Modeling*, 656 pp., Cambridge Univ. Press, New York, 1999a.

Jacobson, M. Z., Isolating nitrated and aromatic aerosols and nitrated aromatic gases as sources of ultraviolet light absorption, *J. Geophys. Res., 104*, 3527-3542, 1999b.

Jacobson, M. Z., Effects of soil moisture on temperatures, winds, and pollutant concentrations in Los Angeles, *J. Appl. Meteorol., 38*, 607-616, 1999c.

Jacobson, M. Z., A physically-based treatment of elemental carbon optics: Implications for global direct forcing of aerosols, *Geo. Res. Lett, 27*, 217-220, 2000.

Jacobson, M. Z., Global direct radiative forcing due to multicomponent anthropogenic and natural aerosols, *J. Geophys. Res., 106*, 1551-1568, 2001.

Jacobson, M. Z., GATOR-GCMM: 2. A study of day- and nighttime ozone layers aloft, ozone in national parks, and weather during the SARMAP field campaign, *J. Geophys. Res.*, this issue.

Jacobson, M. Z., R. Lu, R. P. Turco, and O. B. Toon, Development and application of a new air pollution modeling system, part I, Gas-phase simulations, *Atmos. Environ., 30(B)*, 1939-1963, 1996.

Jakobs, H. J., H. Feldmann, H. Hass, and M. Memmesheimer, The use of nested models for air pollution studies: An application of the EURAD model to a SANA episode, *J. Appl. Meteorol., 34*, 1301-1319, 1995.

Jones, R. G., J. M. Murphy, M. Noguer, and M. Keen, Simulation of climate change over Europe using a nested regional climate model, II, Comparison of driving and regional model responses to a doubling of carbon dioxide, *Q. J. R. Meteorol. Soc., 123*, 265-292, 1997.

Juang, H.-M. H., and M. Kanamitsu, The NMC nested regional spectral model, *Mon. Weather Rev., 122*, 3-26, 1994.

Kabat, P., R. W. A. Hutjes, and R. A. Feddes, The scaling characteristics of soil parameters: From plot scale heterogeneity to subgrid parameterization, *J. Hydrol., 190*, 363-396, 1997.

Kondo, J., N. Saigusa, and T. Sato, A parameterization of evaporation from bare soil surface, *J. Appl. Meteorol., 29*, 385-389, 1990.

Kumar, N., M. T. Odman, and A. G. Russell, Multiscale air quality modeling: Application to southern California, *J. Geophys. Res., 99*, 5385-5397, 1994.

Kurihara, Y., and M. A. Bender, A numerical scheme to treat the open lateral boundary of limited area model, *Mon. Weather Rev., 111*, 445-454, 1983.

Laprise, R., D. Caya, M. Giguere, G. Bergeron, H. Cote, J. P. Blanchet, G. J. Boer, and N. A. McFarlane, Climate and climate change in western Canada as simulated by the Canadian Regional Climate Model, *Atmos. Ocean, 36*, 119-167, 1998.

Lee, T. J., and R. A. Pielke, Estimating the soil surface specific humidity, *J. Appl. Meteorol., 31*, 480-484, 1992.

Leung, L. R., and S. J. Ghan, Pacific Northwest climate sensitivity simulated by a regional climate model driven by a GCM, part I, Control simulation, *J. Clim., 12*, 2010-2030, 1999.

Liang, J., and M. Z. Jacobson, Comparison of a 4000-reaction chemical mechanism with the Carbon Bond IV and an adjusted Carbon Bond IV-EX mechanism using SMVGEAR II, *Atmos. Environ., 34*, 3015-3026, 2000.

Lide, D. R. (Ed.), *CRC Handbook of Chemistry and Physics*, CRC Press, Boca Raton, Fla, 1998.

Louis, J.-F., A parametric model of vertical eddy fluxes in the atmosphere, *Boundary Layer Meteorol., 17*, 187-202, 1979.

Lozej, C., and R. D. Bornstein, The importance of nesting and initial conditions: MM5 application to a winter storm, in *Preprints of Eighth Conference on Mesoscale Processes*, Am. Meteorol. Soc., Boston, Mass., 1999.

Lu, R., and R. P. Turco, Air pollutant transport in a coastal environment, part I, Two-dimensional simulations of sea-breeze and mountain effects, *J. Atmos. Sci., 51*, 2285-2308, 1994.

Lu, R., and R. P. Turco, Air pollutant transport in a coastal environment, II, Three-dimensional simulations over Los Angeles basin, *Atmos. Environ., 29*, 1499-1518, 1995.

Marinucci, M. R., F. Giorgi, M. Beniston, M. Wild, P. Tschuck, A. Ohmura, and A. Bernasconi, High resolution simulations of January and July climate over the western alpine region with a nested regional modeling system, *Theor. Appl. Climatol., 51*, 119-138, 1995.

Martien, P., and T. Umeda, Cloud cover and mesoscale surface properties derived from AVHRR satellite data to supplement SARMAP field observations in regional photochemical and modeling studies, vol. 1, in *Results and Interpretation of Field Measurements*, edited by A. J. Ranzieri and P. A. Solomon, A&WMA VIP-48, pp. 265-284, Air & Waste Manage. Assoc., 1993.

Mathur, R., L. K. Peters, and R. D. Saylor, Sub-grid representation of emission source clusters in regional air quality modeling, *Atmos. Environ., 26(A)*, 3219-3238, 1992.

McCumber, M. C., A numerical simulation of the influence of heat and moisture fluxes upon mesoscale circulations, Ph.D. thesis, Univ. of Virginia, Charlottesville, 1980.

McCumber, M. C., and R. A. Pielke, Simulation of the effects of surface fluxes of heat and moisture in a mesoscale numerical model, part I, Soil layer, *J. Geophys. Res., 86*, 9929-9938, 1981.

McGregor, J. J., Regional climate modeling, *Meteorol. Atmos. Phys., 63*, 105-117, 1997.

McGregor, J. J., and K. J. Walsh, Nested simulations of perpetual January climate over the Australian region, *J. Geophys. Res., 98*, 23,283-23,290, 1993.

McHenry, J., N. L. Seaman, C. J. Coats, A. Lario-Gibbs, J. Vukovich, N. Wheeler, and E. Hayes, Real-time nested mesoscale forecasts of lower tropospheric ozone using a highly optimized coupled numerical prediction system. in *Preprints of AMS Symposium on Interdisciplinary Issues in Atmospheric Chemistry*, Am. Meteorol. Soc., Boston, Mass., 1999.

Mihailovic, D. T., B. Rajkovic, B. Lalic, and L. Dekic, Schemes for parameterizing evaporation from a non-plant-covered surface and their impact on partitioning the surface energy in land-air exchange parameterization, *J. Appl. Meteorol., 34*, 2462-2475, 1995.

Miller, D. A., and R. A. White, A conterminous United States multi-layer soil characteristics data set for regional climate and hydrology modeling. *Earth Inter., 2*, 1998.

Mlawer, E. J., S. J. Taubman, P. D. Brown, M. J. Iacono, and S. A. Clough, Radiative transfer for inhomogeneous atmospheres: RRTM, a validated correlated-*k* model for the longwave, *J. Geophys. Res., 102*, 16,663-16,682, 1997.

Morris, R. E., M. A. Yocke, T. C. Myers, and V. Mirabella, Overview of the variable-grid urban airshed model (UAM-V), paper presented at the 85th A&WMA Meeting and Exhibition, Air & Waste Management Assoc., Kansas City, Missouri, 1992.

National Aeronautics and Space Administration (NASA), Greenhouse effect detection experiment (GEDEX) selected data sets, NASA Clim. Data Sys. Staff, Goddard Space Flight Cent., Greenbelt, Md., 1992.

Noilhan, J., and S. Planton, A simple parameterization of land surface processes for meteorological models, *Mon. Weather Rev., 117*, 536-549, 1989.

Odman, M. T. and C. L. Ingram, Multiscale Air Quality Simulation Platform (MAQSIP): Source code documentation and validation, *ENV-96TR002-v1.0*, 1996. (Available from MCNC, Research Triangle Park, N. C.)

Oke, T. R., *Boundary Layer Climates*, Methuen, New York,, 1978.

Oke, T. R., R. A. Spronken-Smith, E. Jauregui, and C. S. B. Grimmond, The energy balance of central Mexico City during the dry season, *Atmos. Environ., 33*, 3919-3930, 1999.

Parkinson, C. L., and W. M. Washington, A large-scale numerical model for sea ice, *J. Geophys. Res., 84*, 311-337, 1979.

Pielke, R. A., *Mesoscale Meteorological Modeling*, Academic, San Diego, Calif., 1984.

Pielke, R. A., et al., *Meteorol. Atmos. Phys., 49*, 69-91, 1992.

Platt, C. M. R., A parameterization of the visible extinction coefficient of ice clouds in terms of the ice/water content, *J. Atmos. Sci., 54*, 2083-2098, 1997.

Pleim, J. E., J. S. Chang, and K. Zhang, A nested grid mesoscale atmospheric chemistry model, *J. Geophys. Res., 96*, 3065-3084, 1991.

Podzun, R., A. Cress, D. Majewski, and V. Renner, Simulation of

European climate with a limited area model, part II, AGCM boundary conditions, *Contrib. Atmos. Phys.*, *68*, 205-225, 1995.

Qian, Y., and F. Giorgi, Interactive coupling of regional climate and sulfate aerosol models over eastern Asia, *J. Geophys. Res.*, *104*, 6477-6499, 1999.

Qian, J.-H., F. Giorgi, and M. S. Fox-Rabinovitz, Regional stretched grid generation and its application to the NCAR RegCM, *J. Geophys. Res.*, *104*, 6501-6513, 1999.

Sellers, P. J. S. O. Los, C. J. Tucker, C. O. Justice, D. A. Dazlich, G. J. Collatz, and D. A Randall, A revised land surface parameterization (SiB2) for atmospheric GCMs, part II, The generation of global fields of terrestrial biophysical parameters from satellite data, *J. Clim.*, *9*, 706-737, 1996.

Thompson, N., Barrie, and M. Ayles, The meteorological office rainfall and evaporation calculation system: MORECS. *Hydrol. Memo.*, *45*, 1-69, 1981.

Toon, O. B., C. P. McKay, T. P. Ackerman, and K. Santhanam, Rapid calculation of radiative heating rates and photodissociation rates in inhomogeneous multiple scattering atmospheres, *J. Geophys. Res.*, *94*, 16,287-16,301, 1989.

United States Geological Survey (USGS)/University of Nebraska, Lincoln/European Commission Joint Research Center 1-km resolution global land cover characteristics database, derived from advanced very high resolution radiometer (AVHRR) data from the period April 1992 to March 1993, 1999.

Walcek, C. J., and N. M. Aleksic, A simple but accurate mass conservative, peak-preserving, mixing ratio bounded advection algorithm with Fortran code, *Atmos. Environ.*, *32*, 3863-3880, 1998.

Walmsley, J. L., and M. L. Wesely, Modification of coded parameterizations of surface resistances to gaseous dry deposition, *Atmos. Environ.*, *30(A)*, 1181-1188, 1996.

Welch, R. M., S. K. Cox, and J. M. Davis, *Solar Radiation and Clouds*, Meteorol. Monog. Ser., vol. 17, Am. Meteorol. Soc., Boston, Mass., 1980.

Wesely, M. L., Parameterization of surface resistances to gaseous dry deposition in regional-scale numerical models, *Atmos. Environ.*, *23*, 1293-1304, 1989.

Zeng, X., M. Zhao, and R. E. Dickinson, Intercomparison of bulk aerodynamic algorithms for the computation of sea surface fluxes using TOGA COARE and TAO data, *J. Clim.*, *11*, 2628-2644, 1998.

M. Z. Jacobson, Department of Civil and Environmental Engineering, Terman Engineering Center, Room M-13, Stanford University, Stanford, CA 94305-4020. (e-mail: jacobson@ce.stanford.edu)

(Received January 27, 2000; revised August 22, 2000; accepted August 29, 2000.)